Carbonate Carbon Isotope Chemostratigraphy from the Ruby Ranch Member of the Cedar Mountain Formation in the Western San Rafael Swell

By
Amy Gottberg

Submitted to the graduate degree program in Geology and the Graduate Faculty of the University of Kansas in partial fulfillment of the requirements for the degree of Master of Science.

_____
Chair: Marina Suarez

_____
Greg Ludvigson

_____
Andreas Möller

Date Defended: 01/28/2022

The thesis committee for Amy Gottberg certifies that this is the approved version of the following thesis:

Carbonate Carbon Isotope Chemostratigraphy from the Ruby Ranch Member of the Cedar Mountain Formation in the Western San Rafael Swell

Chair: Marina Suarez

Date Approved: February 1, 2022

Abstract

The Ruby Ranch Member of the Cedar Mountain Formation in East-Central Utah represents terrestrial deposits in the early Cretaceous Period. This member has been studied at multiple field locations and has been determined to span the Aptian-Albian Boundary based on chemostratigraphic and detrital zircon studies. The study location presented here, Moore Cutoff Road, is further west than previous studies, and thought to be a more expanded section that may contribute more detail to the chemostratigraphic and paleoclimatic record. The Ruby Ranch Member in this area consists mainly of reddish grey and greenish gray silty-sandy mudstones with abundant carbonate nodules suggestive of paleosol development. For this study samples were collected approximately every 25 cm and were used to construct a C-isotope curve using carbonate carbon. These were used to compare to existing bulk sedimentary organic carbon isotope curves. A total of 48 samples were analyzed and values from -7.45 ‰ vs. VPDB to -3.52 ‰ vs. VPDB were observed. The C-isotope data follows the trend of existing organic carbon isotope curves which exhibits the C10 positive isotope excursion near the Aptian-Albian boundary. A set of samples have been analyzed for pCO_2 values. These values were calculated using both a high and low value for both S(z) and temperature. pCO_2 values range from 795 ppmV to 2850 ppmV over the 4 scenarios presented. A subset of samples have been analyzed for clumped isotope paleothermometry to test a hypothesis that this positive isotope excursion corresponds with a late Aptian "cold snap" in an otherwise greenhouse climate. This data produced values that were not reliable estimates of temperature. Additional studies are needed to confirm a temperature change over the C10 positive isotope excursion and refine the paleoclimate record at this location

Acknowledgements

I would first like to thank my advisor, Dr. Marina Suarez for all of her help, guidance and patience throughout my time at the University of Kansas. Thank you for taking a chance on me. I would also like to thank Dr. Greg Ludvigson and Dr. Andreas Möller for their insight and support throughout the process. Thank you to everyone who laid the groundwork to make this project possible.

Thank you to my friends who allowed me to talk about this project as much as I needed or wanted to and always supported me. Thank you to Grant Root for his support and encouragement. Finally, a very special thank you to my parents and sister for being so loving and supportive, pushing me to be my best and constantly believing in me.

This project is funded by National Science Foundation grant numbers EAR1925942 and EAR1941017.

Table of Contents

List of Figures

1. Introduction

The Cretaceous Period is geologically important due to greenhouse conditions attributed to increased CO_2 and CH_4 in the atmosphere (Hay, 2011). This period was known for the near complete lack of ice at both of Earth's poles and the latitudinal temperature gradient was less than 30° C, which contrasts current conditions where temperatures between the poles and equatorial areas can reach upwards of 100° C in the southern hemisphere and 50° C in the northern (Hay, 2011). However, there is evidence to suggest cold snaps occurred during the Cretaceous, specifically in the early and mid-Cretaceous, which has been studied using ocean surface temperature data as well as nannofossil records (Bottini & Erba, 2018). Atmospheric CO_2 concentrations within the Ruby Ranch Member have been calculated (Suarez et al., 2020) and need refinement. Atmospheric CO_2 concentrations will be calculated for a portion of the Ruby Ranch Member, which has been suggested to span the Aptian-Albian ages based on prior chemostratigraphic interpretations.

Understanding Cretaceous greenhouse conditions is important to modern climate transitions, which are moving in a warming direction that may approach Cretaceous conditions within 100 years (Hay, 2011). The Cretaceous Greenhouse was likely due to volcanic outgassing, which increased greenhouse gases within the atmosphere and led to an increase in temperature as well as an accelerated hydrologic cycle (Ufnar et al., 2004; Suarez et al., 2011; Ludvigson et al., 2015). The conditions (warm temperatures, relatively high sea level) during the Cretaceous were favorable for numerous Ocean Anoxic Events (OAEs) that represent carbon cycle perturbations (significant shifts in the flux of carbon from one or more reservoir to another) and can be identified by variations in carbon isotope values (Jenkyns, 2010). OAEs are thought to be caused by an abrupt rise in temperature and rapid CO_2 influx from sources such as volcanic outgassing.

There are three main OAEs that fall within the Aptian-Albian time frame: 1a, and 1b, with 1c being less specifically defined due to patchy records. OAE 1a occurred in the early Aptian (~120 Ma) and 1b in the late Aptian to early the Albian (~111 Ma) (Jenkyns, 2010). The variations in carbon isotope values that often accompany OAEs are called Carbon Isotope Excursions (CIEs) (Scholle and Arthur, 1980).

The late Aptian to early Albian in marine sections includes a number of organic rich units comprising OAE 1b (McAnena et al., 2013; Bodin et al., 2015). Paleoclimate data from coeval strata suggest that the temperature decreased during OAE 1b, though some abrupt temperature increases are also thought to have occurred (McAnena et al., 2013; Bodin et al., 2015). C-isotope chemostratigraphy has been used to identify coeval strata in the continentally-derived Cedar Mountain Formation. The Cedar Mountain Formation (CMF) in Utah likely encompasses more than 30 million years (Ludvigson et al., 2015). During this time, strata of the CMF document some of the earliest Cretaceous continental deposits in North America but include strata that signal the advance of the Western Interior Seaway (Kirkland et al., 1997; Ludvigson et al., 2015).

The Ruby Ranch Member (RRM) of the Cedar Mountain Formation has been characterized chemostratigraphically in multiple localities east of the study area, suggesting a late Aptian to early Albian age (Ludvigson et al., 2010; Ludvigson et al., 2015). The study area for this project is the western-most and one of the thicker exposures of the RRM (figure 1) and creates a unique opportunity to compare chemostratigraphic sections and paleoclimate proxies with those farther east (Price River, Ruby Ranch Road) (Kirkland et al., 2016). The carbonate-nodule rich Ruby Ranch Member provides a climate archive to determine if climate changes identified in marine sections are reflected in continental records. The goals of this project were to

improve upon the existing chemostratigraphy, thoroughly evaluate the carbonate nodules previously collected for the use of clumped isotope paleothermometry and calculate pCO_2 values.

2. Background Geology

2.1 Cedar Mountain Formation Members

This study focused on the Cedar Mountain Formation along the western extent of the formation in central Utah, specifically the Ruby Ranch Member (figure 1). The Cedar Mountain Formation has 6 members from bottom to top, the Buckhorn Conglomerate Member, the Yellow Cat Member, the Poison Strip Member, the Ruby Ranch Member, the Short Canyon Member and the Mussentuchit Member (Kirkland et al., 2016). Four of these members are exposed at the study location, Moore Cutoff Road, the Yellow Cat Member, the Ruby Ranch Member, the Short Canyon Member and the Mussentuchit Member.

The oldest member, the Buckhorn Conglomerate, consists of chert pebbles to cobbles derived from Paleozoic strata and is up to 25 meters thick, representing fluvial deposits (Kirkland et al., 1997). This member is exposed in the central portion of the San Rafael Swell and does not crop out in the Moore Cutoff Road location.

The next overlying member is the Yellow Cat Member, which has distinct upper and lower portions. The lower Yellow Cat Member consists of a stacked sequence of root-mottled paleosols with distinct lack of carbonate nodules (Kirkland et al., 2016). The upper Yellow Cat Member is characterized by fine-grained sediments with calcareous nodules, which are commonly paired with sandstone interbeds, interpreted as fluvio-lacustrine and interfluvial plain deposits (Kirkland et al., 2016). At the Moore Cutoff Road location the Buckhorn Conglomerate is absent and the Yellow Cat Member directly overlies the underlying Jurassic Morrison Formation (Kirkland et al., 1997; Kirkland et al., 2016).

Above, the Poison Strip Member is defined as a complex of well-cemented sandstone beds interpreted to be fluvial and interfluvial deposits. The Poison Strip Member is primarily exposed in Eastern reaches of the CMF (Kirkland et al., 2016).

The Ruby Ranch Member is the most consistently expressed of the members in the CMF and thickens to the west and northwest, it is between 15 and 30 meters thick (Kirkland et al., 2016). The Ruby Ranch Member has abundant large carbonate nodules within pale green and purple calcareous mudstone and sandstones, which make finding fossils difficult. These carbonate nodules are interpreted to have developed in paleosols and in ephemeral ponds (palustrine deposits) formed under semiarid conditions (Ludvigson et al., 2015; Kirkland et al., 2016). The member has many ribbon sandstone beds interbedded with calcareous mudstones representing low sinuosity river deposits. This member is known for its distinct dinosaur fossils as they differ greatly from the other members and include dinosaurs such as nodosaurid ankylosaurs, basal iguanodontian tenontosaurs and slender-toothed titanosauriform sauropods (Kirkland et al., 2016).

The Short Canyon Member has a discontinuous pebble to cobble conglomerate lithology, there are up to three conglomerate beds separated by slope-forming sandstones and shales. This member has a thickness of 12 to 32 meters and is primarily exposed in the western end of the San Rafael Swell (this study area) (Kirkland et al., 2016).

Finally, the Mussentuchit Member is the uppermost member of the Cedar Mountain Formation and is present primarily along the west side of the San Rafael Swell (Kirkland et al., 1997; Kirkland et al., 2016). It is distinguished by the abundance of smectitic clays within mudstone beds and the noticeable lack of carbonate nodules. The Mussentuchit Member also contains low grade coal beds (Kirkland et al., 2016).

The Yellow Cat, Poison Strip and Ruby Ranch Members have been investigated extensively using chemostratigraphic, chronostratigraphic and stable isotope approaches as well as paleontological studies (e.g. Ludvigson et al., 2010; Ludvigson et al., 2015; Joeckel et al., 2019, Suaerz et al. 2020). The chronostratigraphy of the Ruby Ranch Member has been constrained using detrital zircon ages, analyses of U-Pb in authigenic carbonate (below the RRM), and carbon isotope chemostratigraphy (Ludvigson et al., 2010; Ludvigson et al., 2015). Ludvigson et al. (2010) reported U-Pb age of 119.4 ± 2.6 Ma for a calcrete located stratigraphically below the RRM, within the Poison Strip Member, and classified the RRM as late Aptian to Albian in age. Lee (2021) suggests the Aptian-Albian boundary lies within the upper RRM and refined the age of the RRM as 121.9 ± 1.5 Ma to 107.1 ± 1.1 Ma and specifically refined the age of the C10 positive isotope excursion to 118.1 ± 2.3 Ma and 119.7 ± 0.7 Ma.

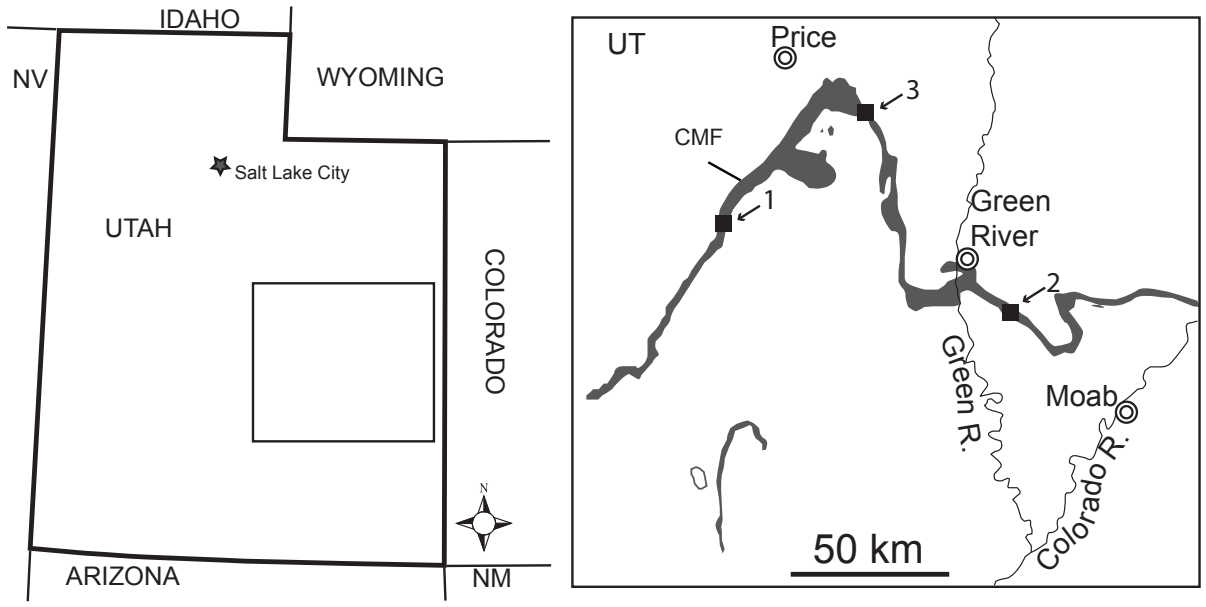

Figure 1: Location map showing the Cedar Mountain Formation in dark grey. Locality 1 shows the field site for this study, locality 2 shows the type section for the Ruby Ranch Member and locality 3 shows the location of the Price River section. Image modified from Ludvigson et al., 2010.

The Ruby Ranch Member outcrop located at Moore Cutoff Road (approximately 10.5 km north of Interstate 70, and 7.5 km southeast of Moore, Emery County, Utah) is the focus of this study (Figure 1). McColloch (2019) utilized bulk sedimentary organic carbon $\delta^{13}C$ values to identify the C10 C-isotope segment between about 13 and 30 meters from the base of the Ruby Ranch Member at this locality. This preliminary chemostratigraphic profile along with newly collected samples form the basis of this project.

3. Methods

3.1 Field Work

Prior bulk sedimentary organic C chemostratigraphic curve was completed from the base of the Ruby Ranch Member to approximately 10 meters below the contact between the Ruby Ranch Member and overlying Short Canyon Conglomerate (McColloch, 2019). Field work was conducted in October 2020 to complete this remaining section. Samples were collected at intervals of ~ 25 cm and lithologic descriptions were completed for the top of the Ruby Ranch Member, totaling 9.21 meters. Observations of color, lithology, sedimentary structures and the presence of any fossils were recorded. Two trenches were dug to ensure non-weathered hand samples were collected. The entirety of the Ruby Ranch Member was re-measured to fix discrepancies within 2017 field notes (Table 4).

3.2 Organic Carbon Isotope Analysis

Samples were crushed to a fine powder and decarbonated using 3M hydrochloric acid upon return to the laboratory. After rinsing samples to neutrality and drying, samples were weighed into 4 x 6mm tin capsules (50 mg to 90 mg depending on % C). Samples were combusted on a Costech 4010 elemental analyzer connected via continuous flow to a ThermoFinnigan MAT 253 IRMS at the Keck Paleoenvironmental and Environmental Stable Isotope Laboratory at the University of Kansas. Carbon isotope values are corrected to VPDB scale using internal and international standards (USGS24, DORM, ANU, IAEA-600) and reproducibility is reported at ± 0.11‰.

3.3 Thin Section Analysis

Thin sections were previously prepared from 42 samples obtained from this site in 2017 and were used to help interpret specific environments that formed the carbonates and mudstone

matrix as well as to evaluate diagenesis. The thin sections were analyzed using plane-polarized and cross-polarized light on an Olympus BX43P petrographic microscope with a SC50 Olympus camera at the University of Kansas. They aided in identifying carbonate mineralogy and textures throughout as well as primary and secondary sedimentary features. Samples have been categorized based on the observed main carbonate textures, noted in table 5 (microcrystalline calcite (micrite), microsparite, sparite, etc.). Evidence for primary carbonate include micrite, evidence of pedogenesis such as root traces, meniscus cements, and circumgranular cracking. Evidence of later carbonate phases include crystal coarsening (microspar to spar), fractures and vein and void filling sparry cements. These features helped identify samples most appropriate for clumped isotope analyses.

3.4 Cathodoluminescence Imaging

Macroscopic Cathodoluminescence (CL) imaging was used to aid in the interpretation of 5 thin sections chosen for clumped isotope analyses and to help identify different generations of carbonate production, which produce varying degrees of orange luminescence, as well as make sedimentary features more apparent. The samples were CL imaged at the Kansas Geological Survey using a Relion Industries Reliotron III cold cathode chamber under rarified He atmosphere at 50 MTorr, an acceleration voltage of 10 kV and beam current of 0.5 mA. CL microphotography was captured using an Olympus DP73 17 Megapixel digital camera on a modified Olympus BX41 microscope and macrophotography was taken using a 16 Mpx Canon EOS SL1 DSLR camera with the lens suspended over the CL chamber.

3.5 Stable Isotope Analysis

In addition to thin sections and CL imaging, oxygen and carbon isotopes aided in interpretation of environments and diagenesis. C-isotopes reflect the dissolved inorganic carbon

that precipitated the carbonates and the oxygen isotopes reflect both the temperature of precipitation and the oxygen isotope composition of precipitating water. Clumped isotopes provide temperatures at which carbonates were precipitated, for details see section 3.6.

48 samples were analyzed for carbonate $\delta^{18}O$ and $\delta^{13}C$, and 6 samples were used for clumped isotope analyses. Carbon and oxygen isotope values were plotted on X-Y graphs and patterns and values compared with carbonate phases observed in thin section. The carbonate phases that showed abundant homogenous micrite with low $\delta^{13}C$ and $\delta^{18}O$ variability indicated little evidence of late diagenetic overprinting (see below) were microdrilled and powder samples were collected for clumped isotope analysis.

Traditional carbon and oxygen isotope analyses were completed using the Thermo Kiel IV Carbonate Device at the University of Kansas. Approximately 70 micrograms of drilled powder samples were roasted at 200°C under vacuum for one hour. After these samples were roasted, they were moved into vials for the Kiel device. These vials were placed within a carousel with 6 reference standard samples. The Kiel device is temperature controlled, which allows the reactions to take place at 72°C. The atmosphere within each individual vial is evacuated creating a vacuum, after this occurs the change in pressure is measured within the vials. The device drops phosphoric acid into the vials producing CO_2. Cryogenic purification removes non-CO_2 contaminants such as water vapor. The CO_2 is then transferred to the sample side bellow of the ThermoFinnigan MAT 253 dual inlet isotope ratio mass spectrometer (IRMS). This is repeated for all of the powdered samples and standards. The samples were analyzed with NBS-18 and or NBS-19 (internationally accepted carbonate isotope standards), TSF-1, Sigma Calcite and 88b Dolomite (internally calibrated reference materials) reference materials, which

are used to correct unknown samples relative to Vienna Pee Dee Belemnite (VPDB). Reproducibility for $\delta^{13}C$ is reported as 0.04 ‰ and for $\delta^{18}O$ as 0.07‰ in this study.

3.6 Carbonate Clumped Isotope Analysis

Carbonate clumped isotope analysis (Eiler, 2011; Affek, 2012) is a relatively new paleotemperature proxy that analyzes the abundance of heavy carbon (^{13}C) and oxygen (^{18}O) bonded in the carbonate isotopologue. The bonds between these two rare isotopes are more thermodynamically stable at low temperatures. This temperature dependence allows the temperature at the time of precipitation of the carbonate to be determined without assuming the oxygen isotopic composition of the precipitating fluid. The clumped isotope analyses took place at the University of Colorado, Boulder on a Thermo MAT 253 Plus. The clumped isotope analysis follows a similar method of acid digestion (in this case the use of a common acid bath at 90°C) and collection of CO_2 as traditional carbonate carbon and oxygen isotope analyses, but the clumped isotope analyses required measuring all CO_2 isotopologues (m44-m49) and requires larger samples, measuring approximately 5 to 10 mg run in triplicate (approximately 30 milligrams of powder in total). Data was corrected into the absolute reference frame of Dennis et al. (2010) with an additional correction to carbonate standards ETH-1, ETH-2, ETH-3 and ETH-4 (reference for the ETH ref mats).

3.7 pCO_2 Calculations

Atmospheric pCO_2 calculations were done using the equation of Ekart et al. (1999) (eq 1). Variables in the equation are a combination of estimates and assumptions from previous studies (Ekart et al. 1999; Suarez et al., 2020). $\delta^{13}C_s$ and $\delta^{13}C_r$ use collected isotope data from 2017 and 2020. $\delta^{13}C_{atm}$ and S(z) are assumed from previous studies (Ekart et al., 1999; Suarez et al., 2020).

$$pCO_2 = S(z)((\delta^{13}Cs - 1.0044 \times \delta^{13}Cr - 4.4) \div (\delta^{13}Catm - \delta^{13}Cs))$$ **(eq 1)**

$\delta^{13}C_s$ represents the $\delta^{13}C$ value of soil CO_2 that precipitated carbonate nodules. It is calculated from an enrichment factor calculated using temperature (eq 2) subtracted from the carbonate carbon isotope value from Moore Cutoff Road samples. This value was calculated using both a low temperature estimate as well as a high temperature estimate from clumped isotope paleothermometry data from Suarez et al. (2020) of Ruby Ranch Member carbonates at the type section of the Ruby Ranch Member.

$$Enrichment\ Factor = 11.98 - 0.12 \times T(°C)$$ **(eq 2)**

The low temperature value used an acceptable assumption from Ekart et al. (1999) for soils in subtropical to temperate conditions at 25°C. The high temperature value was from Suarez et al. (2020) using clumped isotope data from Ruby Ranch Road, their samples produced the high temperature value of 39°C.

$\delta^{13}C_r$ represents the soil respired CO_2 values, these values come from organic carbon isotope values from the 2017 Moore Cutoff Road samples (McColloch, 2019). $\delta^{13}C_{atm}$, which is representative of atmospheric CO_2, values vary depending on the stratigraphic position of the sample within the section. Ludvigson et al. (2015) reports averaged values of marine carbonates from previous analyses, these marine carbonate averages minus 8, were used in the calculation.

Table 1: Average $\delta^{13}C_{atm}$ for Carbon Isotope Segments

Carbon Isotope Segment	Average $\delta^{13}C_{atm}$ ‰ vs. PDB
Mid C9	-4.87
Peak C10	-4.21
Low Al1	-5.24

S(z) is a depth dependent contribution from soil-respired CO_2 and is a major source of uncertainty in calculating pCO_2. We used both a high, 7000 ppm, and low estimate, 4000 ppm, for S(z) from Ekart et al. (1999), although modern soil studies on vertisols indicate the value for S(z) should be lower, between 1000 and 3000 ppm (Montañez, 2012).

To calculate pCO_2 values from paleosol carbonates, the most appropriate samples should have invariable $\delta^{13}C$ of carbonate values and $\Delta^{13}C$ values should be between 14 and 17‰ (Cotton & Sheldon, 2012). $\Delta^{13}C$ values were calculated by averaging $\delta^{13}C$ values from each carbonate nodule sampled (not including sparry calcite) and subtracting $\delta^{13}C_{org}$ for the equivalent horizon.

4. Results

4.1 Lithostratigraphy

Samples were collected in 2017 and in 2020. The lower section collected in 2017 is detailed in McColloch (2019) and stratigraphic profiles are shown in figure(s) 2 and 3. This 2017 profile was described and collected in 8 trenches and went from the base of the Ruby Ranch Member to about 10 meters below the Short Canyon Conglomerate. The profile in 2020 was collected from the approximate top of the 2017 section to the base of the Short Canyon Conglomerate. 35 samples were collected in 2020. Lithostratigraphically the 2020 section is described as mainly grey sandy or silty mudstone with carbonate nodules in varying amounts. Green mottles were found throughout the trench and at the top orange and green mottles were a dominant feature. Detailed descriptions of the collected samples in 2017 and 2020 are shown in tables 2 and 3. In addition to collecting this upper portion of the Ruby Ranch Member at Moore Cutoff Road, the 2020 collecting session revised the original thicknesses described in McColloch (2019). There were two major sections that were described as skipped sections in McColloch (2019). After revisiting the site, we identified that the previously documented thick missed sections were not in fact covered or skipped section but a result of math errors in addition of thicknesses, these data have been replotted reflecting accurate stratigraphic height. It is important to note, that the sample names and numbers (which referenced cm above the base) will be retained for these samples.

The Ruby Ranch Member at this location (Moore Cutoff Road) can be broken into lithologic facies throughout the thickness. In the lower portion of the section a reoccurring facies (facies 1) can be described as reddish grey sandy, calcareous mudstone. This facies includes carbonate nodules throughout along with green mottles in some of the units and is mainly at the

base of the section through approximately 1450 cm from base of the member. Facies 2 is described as a grey sandy calcareous shale. It has carbonate nodules present and occurs twice in the section, interspersed with facies 1. Facies 3 is a greenish fine sandstone, located between 650 cm and 850 cm. Facies 4 is a grey to black sandy calcareous mudstone with carbonate nodules. This facies is mainly present midway through the section (approx. 1650 cm to 2675 cm). Facies 5 is described as a green-grey sandstone and is noted at approximately 1350 cm to 1550 cm and again at 2350 cm to 2675 cm. Facies 6 occurs twice within the section and is described as a resistant bed made of coalesced carbonate nodules, these are grey and are present immediately underlying lower? occurrence of facies 4. Facies 7 is a tan, resistant calcareous sandstone unit, it is present from approximately 1975 cm to 2025 cm. Facies 8 is a tan-yellow sandy mudstone with orange mottles and carbonate nodules within, that is present from approximately 2900 cm to 3100 cm. Facies 9 is a grey, sandy, calcareous mudstone and sits directly on top of facies 8, it has some carbonate nodules in the lower portion of the facies. Facies 10 is a purple-green mottled calcareous mudstone with carbonate nodules present, it sits directly on top of facies 9 as well as between approximately 880 cm and 1000 cm.

The section measured in 2020 can be broken up into 2 distinct lithofacies. Facies 11 is described as a sandy mudstone, which is green-grey. This section includes carbonate nodules throughout as well as orange resistant carbonate nodules. Orange and green mottles are common within the lower portion of this facies. The uppermost distinct facies (facies 12) is also a sandy mudstone, it is tan, mudcracks are present within this facies.

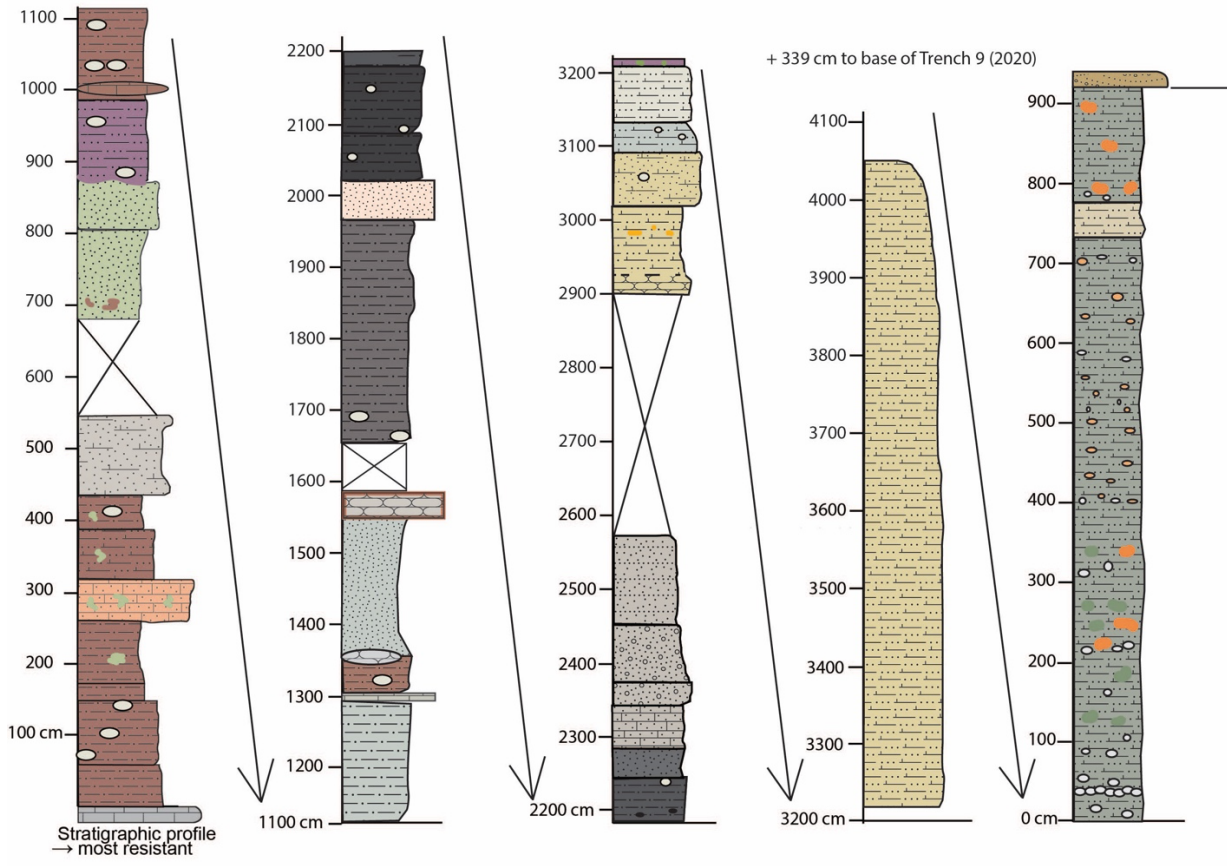

Figure 2: Stratigraphic column showing the section collected in 2017 (Samples collected from McColloch 2019) Figure 3 shows stratigraphic column of samples collected in 2020 which lies 339 cm above the top of column shown (4050 cm)

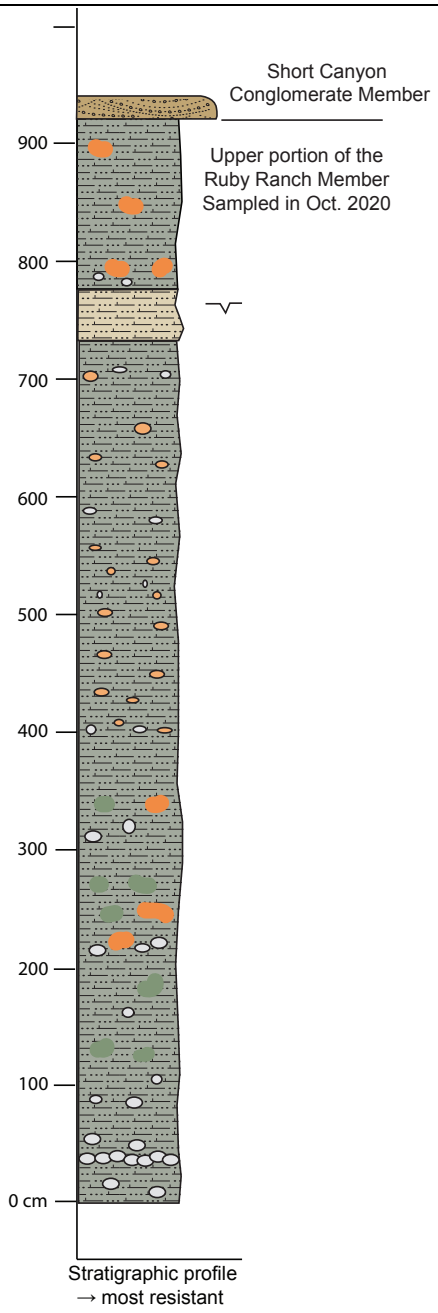

Figure 3: Stratigraphic column showing section collected in 2020

4.2 Petrography and Stable Isotope Geochemistry

Thin section analysis was performed to determine microfacies present within the samples collected in 2017. The composition of the thin sections allows for a greater understanding of environmental conditions responsible for carbonate formation. These thin sections were observed under cross-polarized, plane-polarized light and cathodoluminescence (CL) to determine mineralogic composition of the sample as well as to identify primary and diagenetic features. Variations in CL colors and intensity reveal variability in the incorporation of Mn^{2+}, which is typically related to redox conditions in the precipitating fluids (Hemming et al., 1989; Ludvigson et al., 2010). Variations in CL are therefore an indication of variability in geochemical conditions. There are 13 samples where the matrix is micrite dominated, 12 samples are considered complex and did not have a definite homogeneous matrix and 17 samples are classified as "other", which includes matrix dominated by microspar, sparite or siliciclastic dominated. Samples of all matrix types were drilled for analysis. The categorization of samples from the study location was the starting point for determining which samples to use for clumped isotope and stable isotope analysis.

Samples classified as micritic matrix showed micrite as the main component of the sample. Many of these samples have veins filled with spar or microspar but most of the samples from this category were homogeneous micrite. Eight samples from this category were drilled for stable isotope analysis, chosen mainly due to the amount of the sample available and the ability to drill sample presumed to be unaltered (not recrystallized) material.

The complex matrix category included samples that consistently had micrite in the matrix but also had large quantities of spar or microspar throughout as well as chalcedony. The micrite made up less than ~ 50% of the sample and was mixed in with other minerals, making them

harder to drill samples which could be classified as one type of material. Seven samples classified as complex matrix were drilled for stable isotope analysis, these samples allowed for spar to be drilled individually as well as the micrite and gave values to compare to samples with a more homogeneous micritic matrix.

The final category, "other" encompasses two samples which do not fall into the other categories. One sample shows a matrix made of mainly microspar with large amounts of chalcedony throughout cracks or veins. The second sample has a matrix made of mostly clay and is organic rich.

Although all the drilled samples have different matrix and features the $\delta^{13}C$ and $\delta^{18}O$ values clump together without much variation between groupings, excluding 2 spar samples (Figure 4). Stable isotope analysis on 42 samples produced $\delta^{13}C$ values between -6.96‰ and -3.52‰ and the values for $\delta^{18}O$ ranged between -9.37‰ and -7.5‰ (Table 6). Samples which were micritic throughout made up all but two values, these were found to be within the stated range. Two samples were drilled from spar-filled voids, these samples produced values which were significantly lower than the micritic samples at the respective stratigraphic horizons for both $\delta^{13}C$ and $\delta^{18}O$, these values are -9.5‰ (1352) and -5.27‰ (1650) and -9.03‰ (1352) and -8.54‰ (1650) respectively. One of these samples (1352) was classified as complex and the other (1650) was classified as "other".

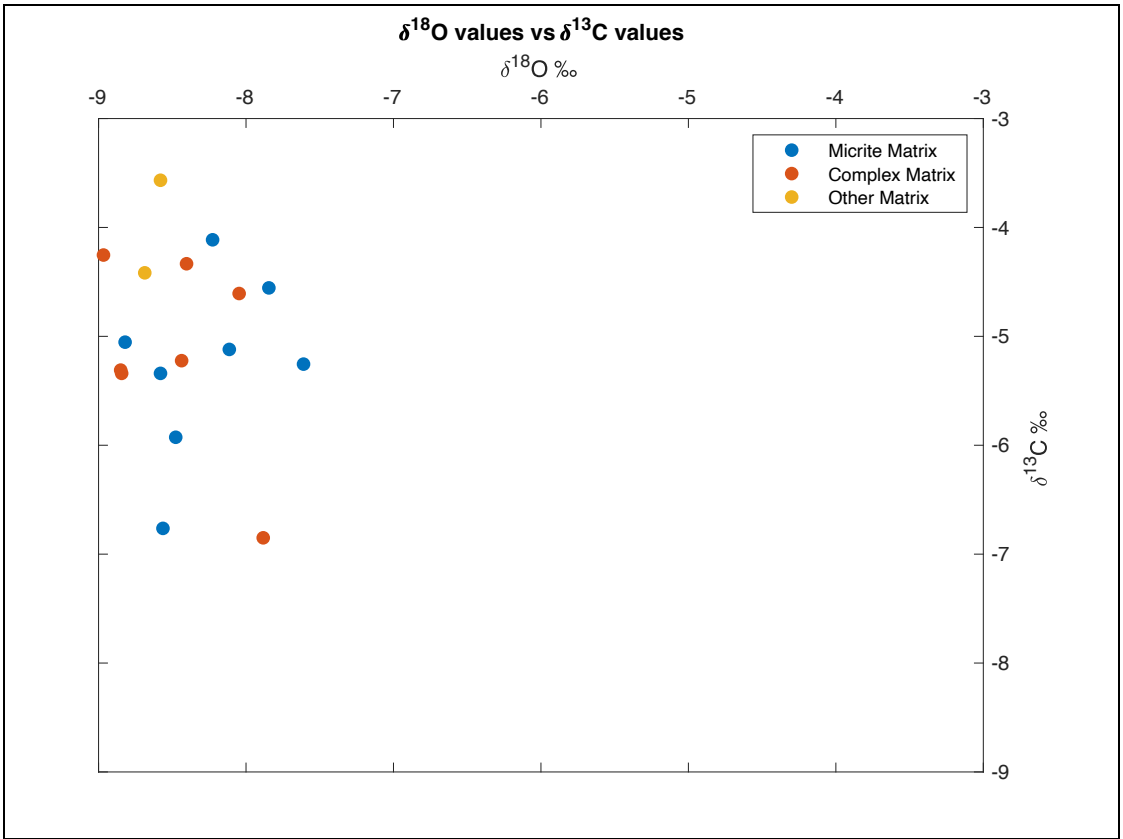

Figure 4: $\delta^{18}O$ versus $\delta^{13}C$ shown by matrix classification of the samples chosen for CL imaging (100, 880, 1152, 1352, 1547)

Micrite dominated samples such as 1152 and 1547 have a homogeneous dull orange luminescence when observed as CL macro-images (Figure 5, 6). Oxygen isotope values for these samples average -8.46‰ and range from -8.04 to -8.92‰. Carbon isotope values range from -5.2 to -4.95‰ and averages -5.08‰. Sample 100 is a micrite dominated sample with cracks which luminesce bright yellow in the center but show no luminescence surrounding the crack. This sample has a homogenous dull orange luminescence with a section of darker orange luminescence mottled throughout (Figure 7). This sample has oxygen isotope values which range between -7.72 and -7.5‰ and average -7.61‰. Carbon isotope values range from -5.56 and -4.95‰ and average -5.25‰.

When observed as micro-images these homogeneous samples were revealed to be more complex than previously observed. Sample 100 shows a micritic matrix with a purple luminescence interspersed with bright yellow microspar or small spar calcite crystals and bright blue detrital quartz grains. A crack within the sample shows a very dark purple rim around the crack and mottled yellow and purple color within the center of the crack (Figure 7). Sample 1152 shows a dull orange-purple micritic matrix with dull spar filled voids within, some with a bright yellow luminescence. The vein consists of dark purple luminescent calcite on the edge with a second bright luminescent calcite phase in the center (Figure 5). Sample 1547 has a dull orange matrix with some yellow spar grains and blue quartz grains interspersed within. The veins in this sample are filled with non-luminescent chalchedony. The edge of the vein have a thin rim which are bright yellow. There is some yellow mottling throughout the matrix (Figure 6).

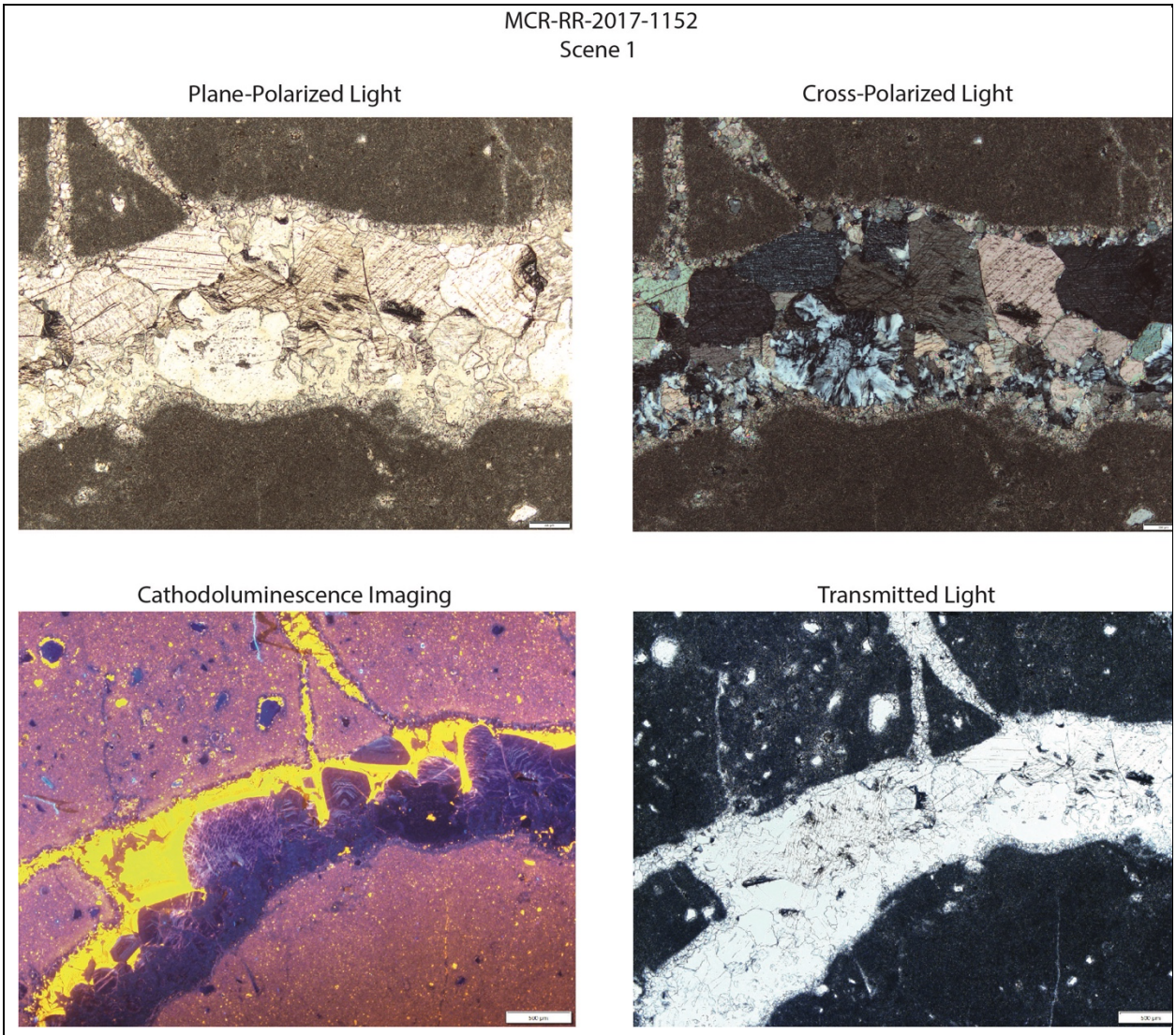

Figure 5: Sample 1152 (scene 1 of 1), which is categorized as micrite-dominated, shown in Cross-Polarized light, Plane-Polarized light, Cathodoluminescence Imaging and Transmitted light. Cathodoluminescence Imaging and Transmitted light photos are taken with a 500 µm scale while the Plane-Polarized and Cross-Polarized photos are taken with a 200 µm scale.

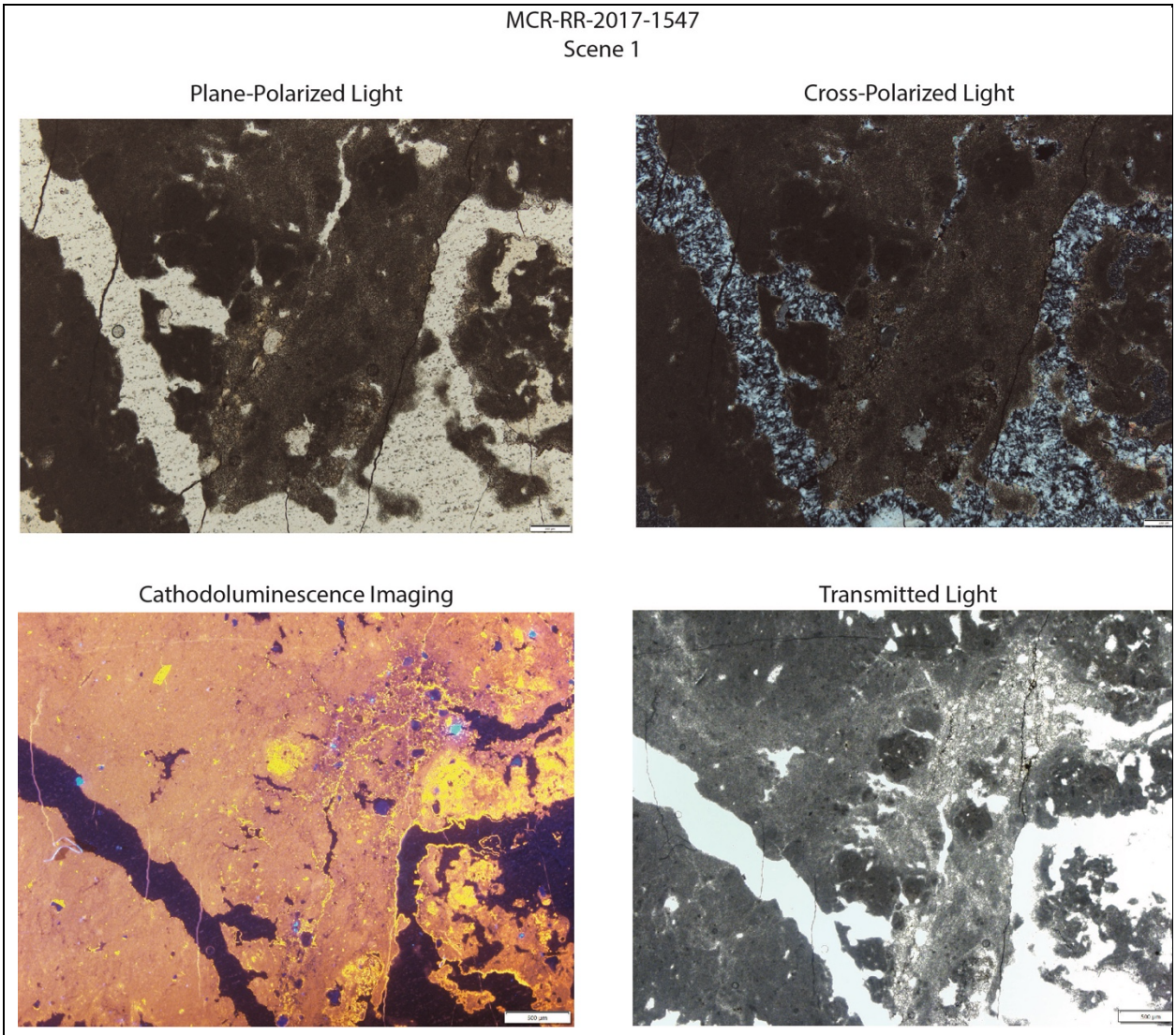

Figure 6: Sample 1547 (scene 1 of 1), which is categorized as micrite-dominated, shown in Cross-Polarized light, Plane-Polarized light, Cathodoluminescence Imaging and Transmitted light. Cathodoluminescence Imaging and Transmitted light photos are taken with a 500 µm scale while the Plane-Polarized and Cross-Polarized photos are taken with a 200 µm scale.

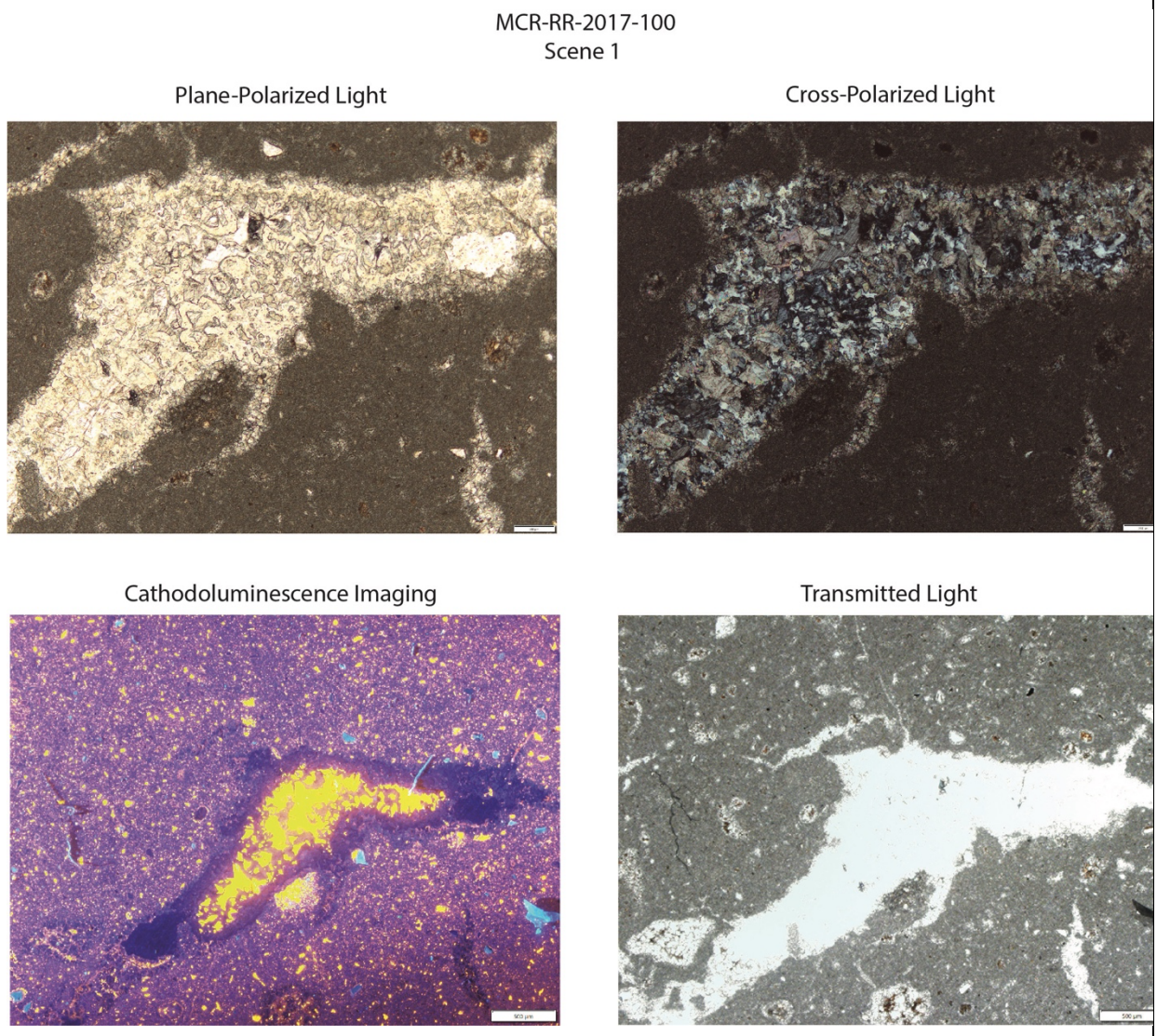

Figure 7: Sample 100 (scene 1 of 2), which is categorized as micrite-dominated, shown in Cross-Polarized light, Plane-Polarized light, Cathodoluminescence Imaging and Transmitted light. Cathodoluminescence Imaging and Transmitted light photos are taken with a 500 µm scale while the Plane-Polarized and Cross-Polarized photos are taken with a 200 µm scale. Sample 100 Scene 2 can be found in Appendix D

The more complex carbonate samples showed varying degrees of luminescence. Samples such as 880 and 1352 show variable luminescence in zoning of vein fill. Some fractures are filled with calcite veins that are brightly luminescent at the edges but with a non-luminescent phase in the center (Figure 8, 9). Others have a non-luminescent phase on the edge, with bright luminescence in the center. The micritic matrix portions of these samples have oxygen isotope values that range between -8.89 and -7.94‰ and average -8.24‰. Carbon isotope values range from -6.27 and -4.09‰ with an average value of -4.92‰. Sample 1352 was sampled in the spar filled vein, values are reported above. The complex samples also appear complex under CL micro-imaging. Sample 880 has a large purple nodule with some bluish luminescent detrital quartz grains. It has a thin yellow edge surrounding it. Mottling is common throughout the sample showing a dull orange-tan color with bright yellow. There are also areas of solid bright yellow. The matrix has a dull orange luminescence (Figure 8). Sample 1352 has an orange luminescent matrix with yellow luminescent authigenic calcite crystals and blue detrital quartz grains within. The veins within this sample are bright yellow in the center and the edge of the vein has a thick dark purple calcitic rim (Figure 9).

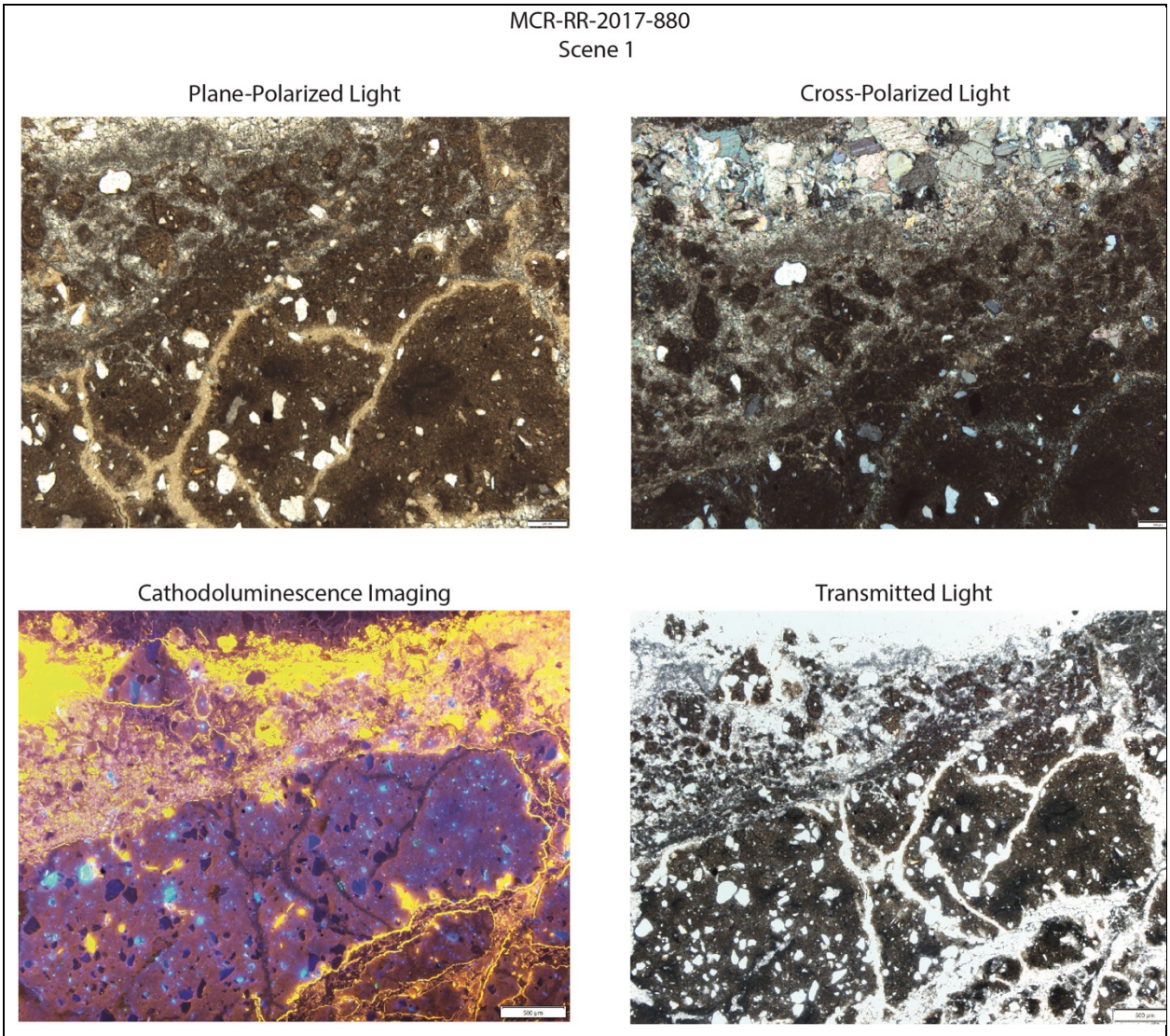

Figure 8: Sample 880 (scene 1 of 2), which is categorized as a complex matrix, shown in Cross-Polarized light, Plane-Polarized light, Cathodoluminescence Imaging and Transmitted light. Cathodoluminescence Imaging and Transmitted light photos are taken with a 500 µm scale while the Plane-Polarized and Cross-Polarized photos are taken with a 200 µm scale. Sample 880 Scene 2 can be found in Appendix D

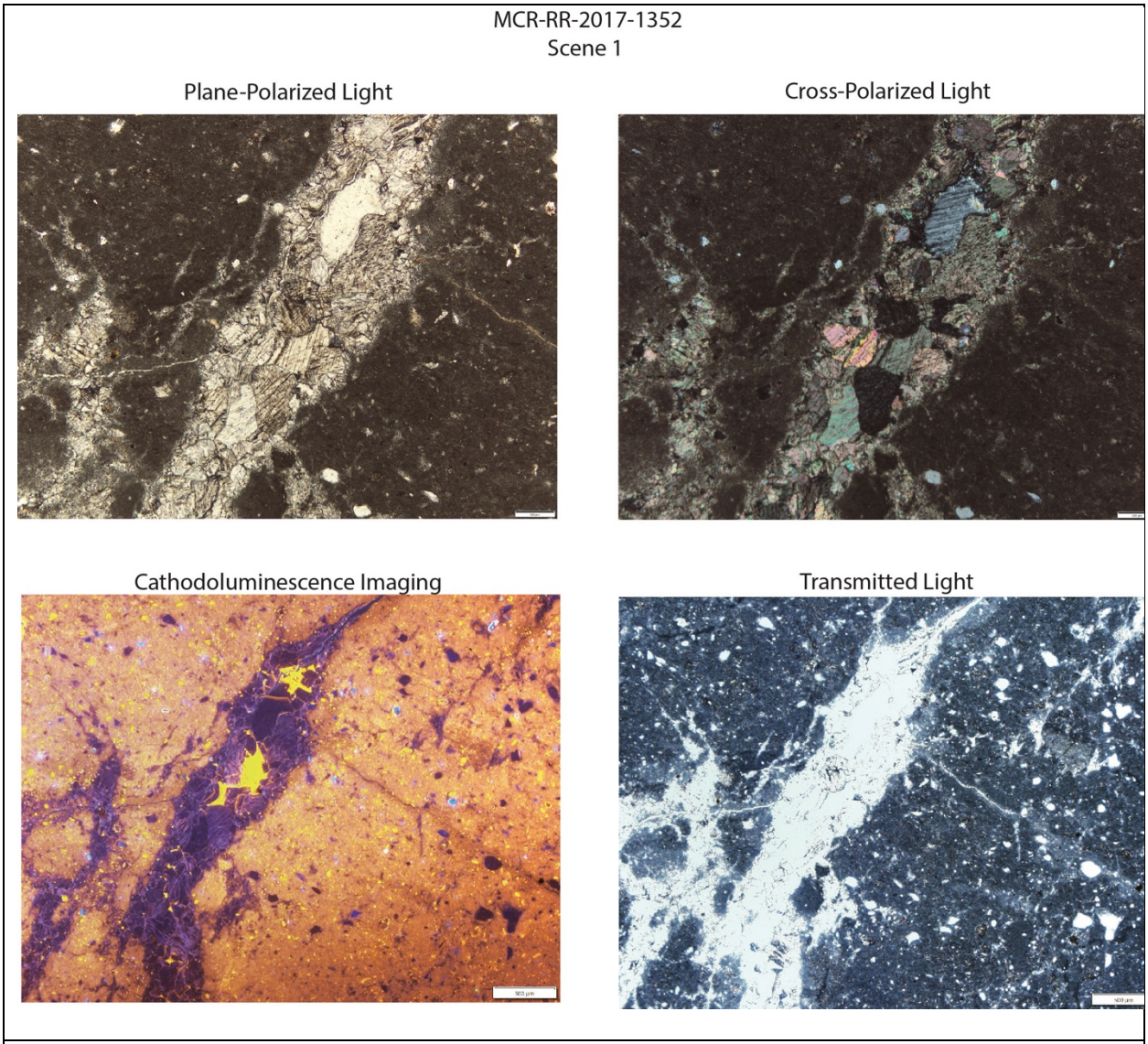

Figure 9: Sample 1352 (scene 1 of 2), which is categorized as a complex matrix, shown in Cross-Polarized light, Plane-Polarized light, Cathodoluminescence imaging and Transmitted light. Cathodoluminescence imaging and Transmitted light photos are taken with a 500 µm scale while the Plane-Polarized and Cross-Polarized photos are taken with a 200 µm scale. Sample 1352 Scene 2 can be found in Appendix D

4.3 Chemostratigraphy

$\delta^{13}C$ and $\delta^{18}O$ values were used to create carbonate chemostratigraphic curves (figures 10, 11), this curve was divided into 8 segments (I through VIII) with segment I being at the base of the member and segment VIII near the top. Each of the analyzed samples had approximately 3 isotope samples taken to determine homogeneity within samples. The values depicted in figure 10 are the averages of the micritic values. The sample names below reflect the corrected stratigraphic heights, original stratigraphic heights are recorded in table 4.

4.3.1 $\delta^{13}C$ Chemostratigraphic Segments

The majority of values within Segment I are steady between -5‰ and -5.5‰ with one value,. significantly more negative (-7.45‰). The average $\delta^{13}C$ value for the segment is -5.58‰. An overall increasing trend occurs from Segment II to IV, interrupted by a short negative excursion (Segment III). Segment II has an increasing trend with a minimum value of -5.54‰ and a maximum value of -4.54‰ between thicknesses 1132 cm and 1302 cm with an average $\delta^{13}C$ value of -4.98‰. Segment III shows a decreasing trend with a minimum $\delta^{13}C$ value of -5.2‰ and a maximum value of -4.52‰ between 1352 cm and 1547 cm. The average $\delta^{13}C$ value for segment III is -4.86‰. Segment IV shows an increasing trend with a minimum value of -5.2‰ and a maximum value of -3.52‰ (the most enriched values of all samples analyzed) between thicknesses 1547 cm and 1650 cm and has an average $\delta^{13}C$ value of -4.34‰.
An overall decreasing trend occurs from Segment V to VII, interrupted by a short positive excursion (Segment VI). Segment V encompasses thickness 1650 cm through 2000 cm, this segment has a decreasing trend with a minimum value of -4.65‰ a maximum value of -3.52‰ and an average value of -3.95‰. Segment VI has an increasing trend with a minimum $\delta^{13}C$ value of -4.65‰ and a maximum value of -3.96‰ with an average $\delta^{13}C$ value of -4.23‰

between 2000 cm and 2100 cm. Segment VII spans from 2100 cm to 3050 cm, the minimum value is -6.96‰ and the maximum value is -3.98‰, the average $\delta^{13}C$ value is -4.92‰. Finally, segment VIII represents an increasing trend and encompasses thickness 3050 cm to 3600 cm the minimum $\delta^{13}C$ value is -6.96‰ and the maximum value is -5.34‰ with an average value of -6.01‰. Segments are shown in figure 10.

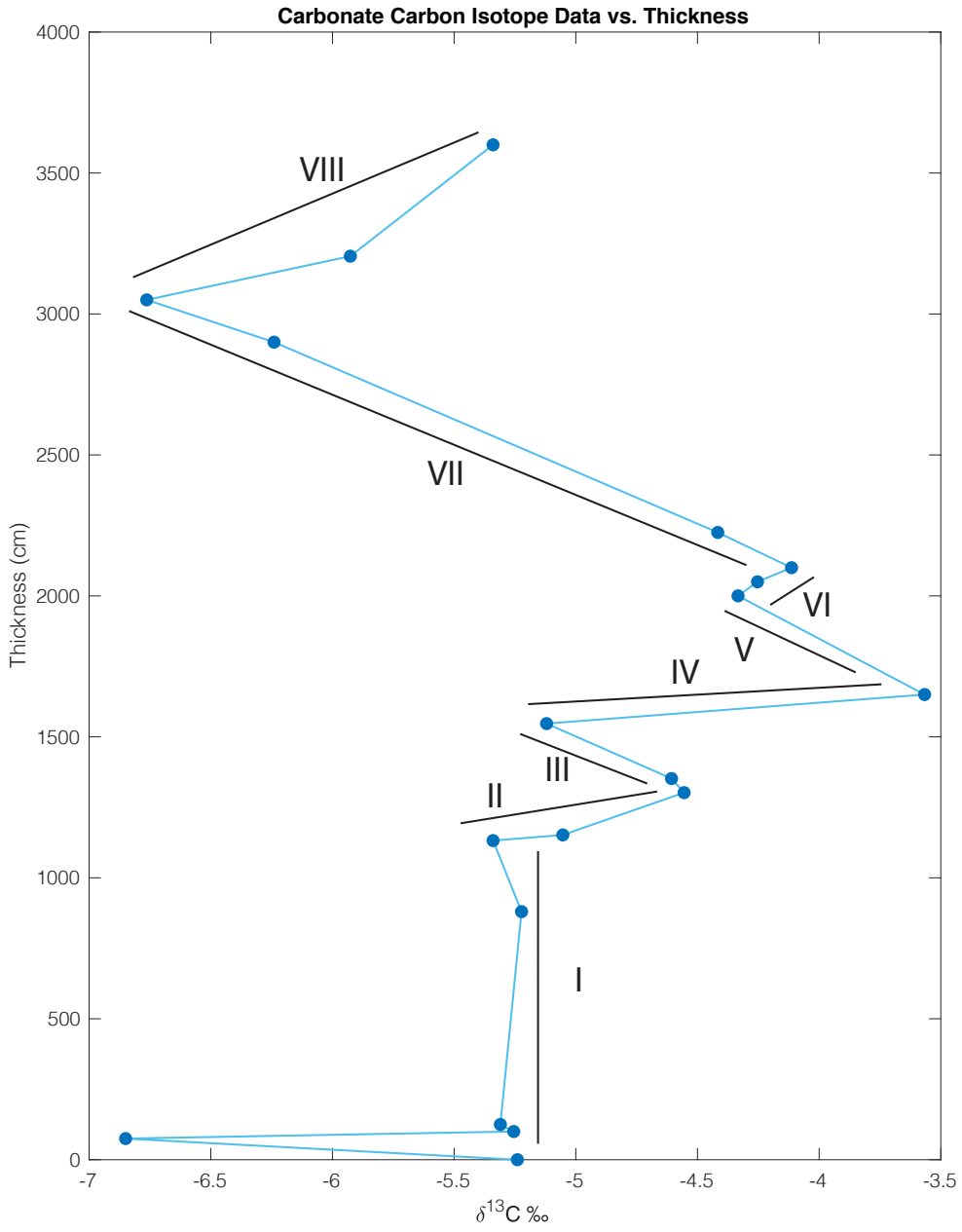

Figure 10: Graph showing $\delta^{13}C$ values against stratigraphic thickness, subdivided into 8 segments described in detail in the text (section 4.3.1). Thickness is from the base of the RRM to top, $\delta^{13}C$ values are from carbonate carbon analysis.

4.3.2 $\delta^{18}O$ Chemostratigraphic Segments

$\delta^{18}O$ values, shown in figure 11, were segmented using the same sections as $\delta^{13}C$ shown in figure 10 (segments I to VIII). Segment I encompasses stratigraphic position 0 cm to 880 cm, the values for $\delta^{18}O$ have a maximum value of -6.72‰ and a minimum value of -8.85‰ with an average $\delta^{18}O$ value of -8.08‰. Segment II, between 1132 cm and 1302 cm, has a maximum value of -7.82‰ and a minimum of -9.02‰ with an average value of -8.50‰. Segment III encompasses thicknesses from 1352 cm and 1547 cm with the maximum $\delta^{18}O$ value -7.94‰ and a minimum value of -8.23‰ with an average $\delta^{18}O$ value of -8.08‰. Segment IV, between 1547 cm and 1650 cm has a maximum value of -8.04‰ and a minimum value of -8.6‰ with an average value of -8.35‰. Segment V encompasses 1650 cm to 2000 cm, the maximum value for this segment is -8.29‰ and the minimum is -8.63‰, the average $\delta^{18}O$ value is -8.49‰. Segment VI spans 2000 cm to 2100 cm with an average $\delta^{18}O$ value of -8.53‰ with a maximum value of -8.02‰ and a minimum value of -9.37‰. Segment VII has an average value of -8.42‰, a maximum value of -8.02‰ and a minimum value of -9.14‰ between thicknesses of 2100 cm and 3050 cm. Finally, segment VIII encompasses 3050 cm to 3600 cm with an average of -8.54‰ with a maximum value of -8.29‰ and a minimum value of -8.87‰. Segments are shown in figure 11.

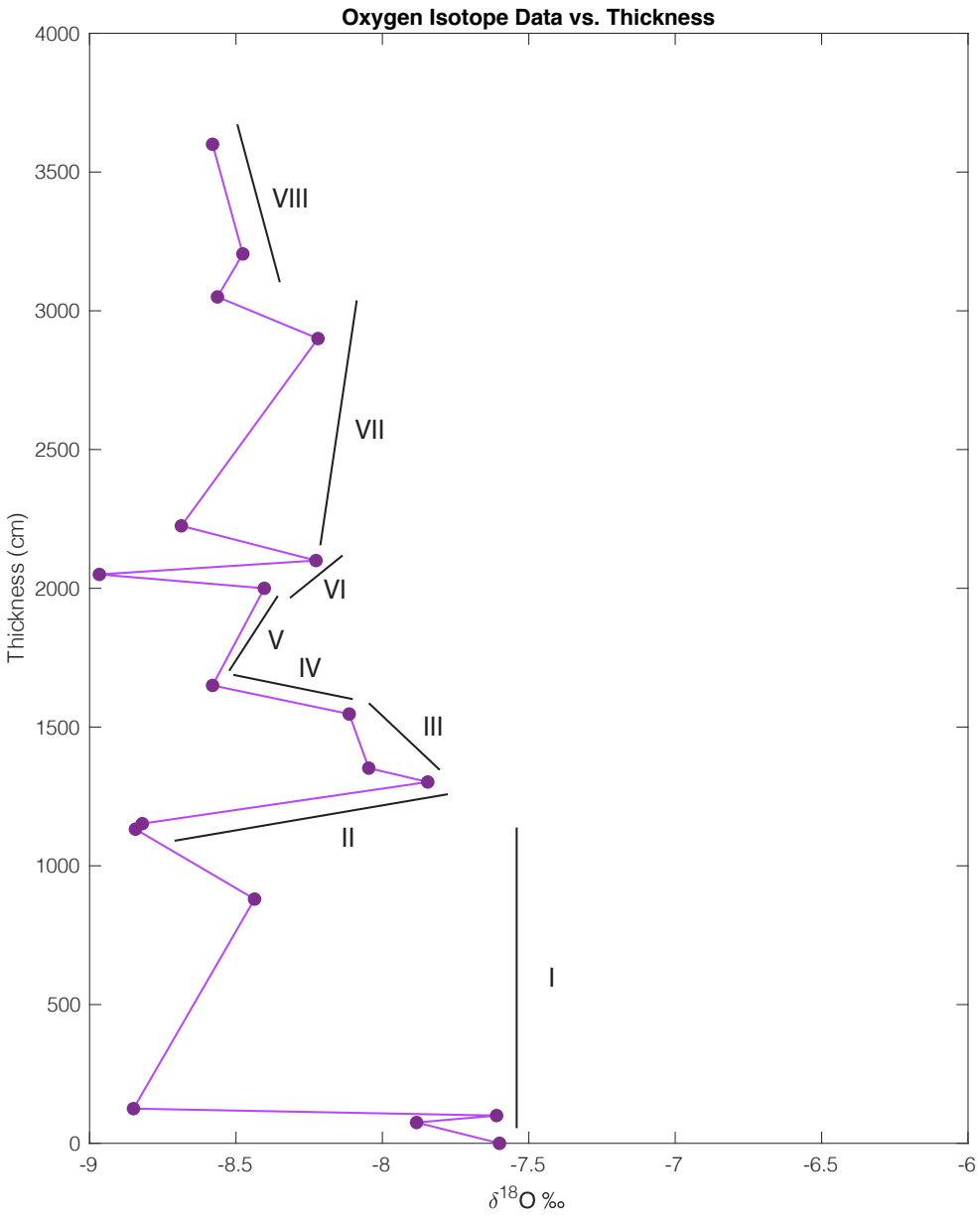

Figure 11: Graph showing $\delta^{18}O$ values against stratigraphic thickness broken into segments based off the graph of $\delta^{13}C$ values (Figure 10)

4.4 Clumped Isotope Geochemistry

Carbonate clumped isotope analysis was completed on 6 samples, 100, 1152, 1547, 2000, 3050 and 5005. None of the samples produced enough CO_2 to analyze in triplicate. Three samples, 100, 1152 and 1547, produced enough CO_2 to be analyzed at least once (sample 1152 was analyzed twice) and produce preliminary temperature data. This data is presented in table 8. With the limited nature of the data, the samples would need to be reanalyzed to produce reliable temperature data. The temperatures however, range from reasonable Earth surface temperatures (34.6 ºC) to temperatures recording reordered or recrystallized processes (64.2 ºC).

4.5 pCO_2 Calculations

pCO_2 calculations were done on 5 samples, 1547, 1650, 2000, 2050 and 3050. Four scenarios are presented using a combination of the variables presented above. Scenario 1 was calculated with a temperature value at 25°C and a S(z) value of 4000 ppm. Scenario 2 was calculated with a temperature value of 25°C and a S(z) of 7000 ppm. Scenario 3 was calculated with a temperature value of 39°C and a S(z) of 4000 ppm and scenario 4 with a temperature value of 39°C and a S(z) of 7000 ppm. Results of these calculations are shown in table 7 for all four scenarios and presented in figure 12.

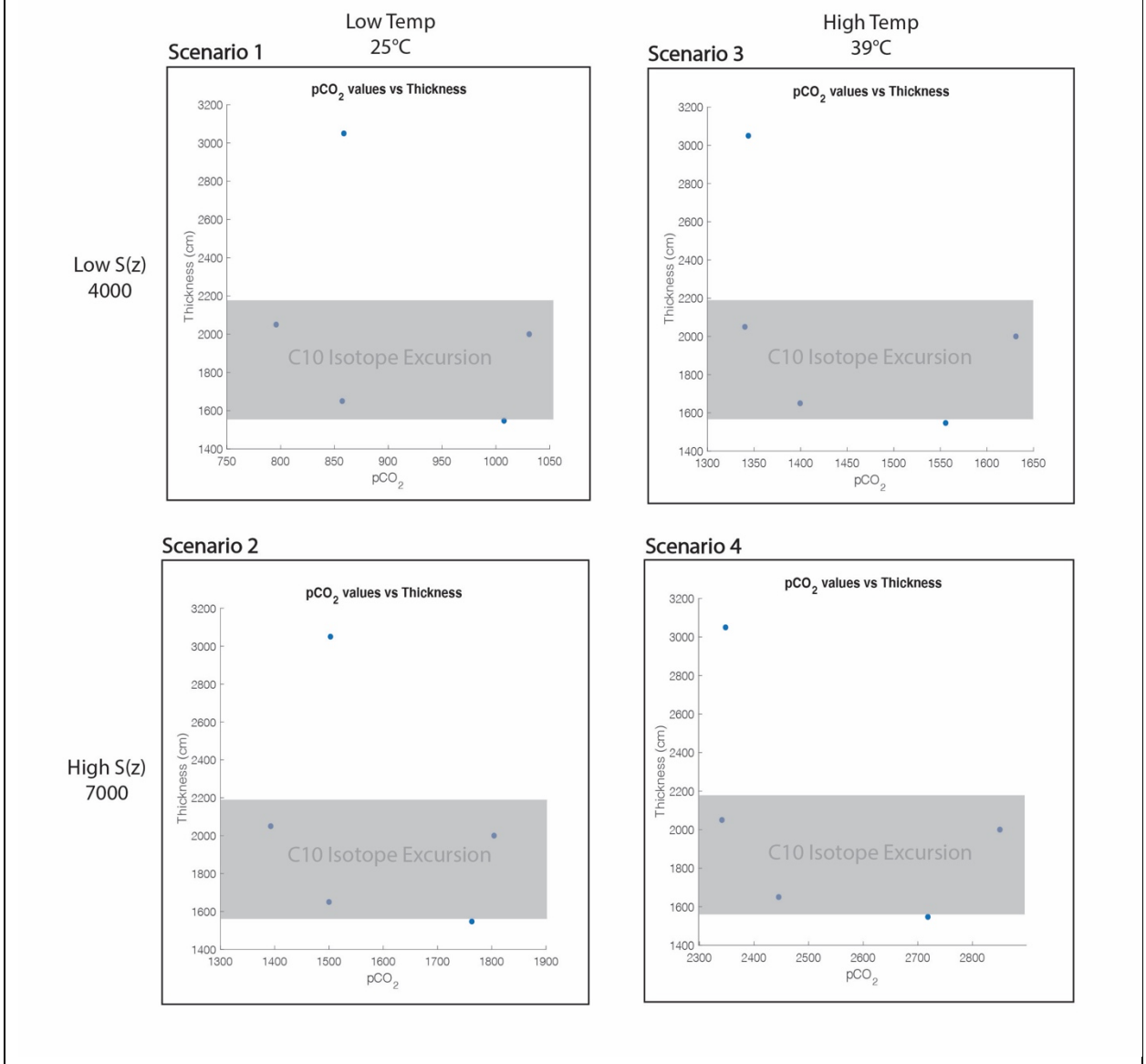

Figure 12: Graphs showing the pCO_2 values at different stratigraphic position using a high and low estimate for temperature and S(z) values. Scenario 1 shows pCO_2 calculations using low temperature of 25ºC and a low S(z) value of 4000 ppm, pCO_2 values range from 795.8 ppmV to 1031.0 ppmV. Scenario 2 shows pCO2 calculations using a low temperature of 25ºC and a high S(z) value of 7000 ppm, pCO_2 values range from 1392.3 ppmV to 1804.2 ppmV. Scenario 3 shows pCO2 calculations using a high temperature of 39ºC and a low S(z) value of 4000 ppm, pCO_2 values range from 1340.1 ppmV to 1631.1ppmV. Scenario 4 shows pCO2 calculations using a high temperature of 39ºC and a high S(z) value of 7000 ppm, pCO_2 values range from 2341.2 ppmV to 2850.2 ppmV. The grey highlighted area shows the identified C10 positive isotope excursion.

5. Interpretations and Discussion

5.1 Interpretations

5.1.1 Lithostratigraphy

The Ruby Ranch Member is known to be a continental deposition system and it is important to know what kind of environment resulted in the lithologies and sedimentary structures at this location. The Ruby Ranch Member was broken up into 12 distinct lithofacies as described previously, each of these facies were formed under specific environmental conditions. Facies 1 can be interpreted to be a calcisol, a soil horizon which is enriched in calcium carbonate or dolomite (Mack et al. 1993). Mottles within can indicate bioturbation or some turning of the soil in the area. The reddish color indicates the presence of oxidized iron within the soil environment. Facies 2 is similar to facies 1 in lithology; it is also a calcitic paleosol with carbonate nodules throughout. The grey color of this facies can indicate the presence of some organic material and/or less well drained conditions. Facies 3 indicates a portion of a modified fluvial system, lack of sedimentary structures does not allow for specific environmental interpretation and/or may suggest bio- or pedo-turbation may have obliterated primary sedimentary features. The color, much like facies 2 indicates organic material. Facies 4 is very similar to facies 2, it is a paleosol with carbonate nodules, the rock within this facies is grey to black in color which indicates a large amount of organics and poorly-drained conditions. Facies 5 is similar to facies 3, but it is more resistant than facies 3 which could indicate a high water table allowing early lithification of the sands. This facies could have reduced conditions, indicated by the dark color. Facies 6 is interpreted as a K horizon within a mature soil. Facies 7 is interpreted as a channel or overbank fluvial area, with minimal organic material and no real structure within. Facies 8 is a paleosol with carbonate nodules which are soil produced. This area

has orange mottles which indicate bioturbation. Facies 9 is a paleosol with some carbonate nodules at the bottom suggesting that the section experienced wet conditions (Kraus, 1999). Facies 10 is a calcitic paleosol with a darker purple color indicating a poorly drained soil. Carbonate nodules are present throughout suggesting drying and wetting periods. This area is highly mottled which indicates bioturbation. Facies 11 is also a paleosol with a large amount of organic material, mottles indicating bioturbation and pedoturbation, and carbonate nodules and orange, resistant, non-calcareous nodules. Facies 12 is a paleosol with some sand content, indicating proximity to a fluvial system. The lack of carbonate nodules indicates an immature soil. This facies also has mud cracks, characteristic for an area which experiences wet and dry conditions where standing water was present at times.

2.1.2 Petrographic Interpretations

Micrite-dominated samples show no evidence of recrystallization and are homogenous. Samples with this matrix type are interspersed throughout this expression of the Ruby Ranch Member. Many of the micrite-dominated samples have cracks or veins that are within the matrix but make up a small percentage of the sample. These cracks are filled with either microspar or spar but these areas are too narrow to sample, these cracks in some areas are thought to be root traces. Root traces are identifiable by smaller cracks branching from a center crack. The edges of many of these cracks show chalcedony. The lack of aquatic fossils within micrite-dominated samples and the presence of suspected root traces suggest these carbonates are most likely pedogenic in origin. The micrite matrix in these samples is the original phase of carbonate. Later phases of calcite are represented by spar and microspar that fill voids left by root traces along with spar filled fractures. CL imaging on this matrix type shows a dull orange luminescence as most of the thin section, this shows the primary phase of calcite as the major component. These

samples show a yellow luminescence at the edges of cracks or voids which can be interpreted to show the later phase calcites such as spar and microspar. Purple coloration, when found within the cracks, seems to be the last carbonate phase.

Complex matrix types show a higher quantity of cracks and voids within usually filled with spar or microspar. Samples in this category show no fossil evidence of aquatic organisms. Many of these samples have chalcedony within voids and fractures that appears to replace the sparry calcite, which indicates dissolution and recrystallization at the edges of these cracks. A spar-filled crack within sample 1352 produced a significantly more negative $\delta^{13}C$ value than the surrounding area indicating some recrystallization. CL imaging of the complex samples includes the previously described dull orange luminescent micrite and the yellow luminescence surrounding the cracks, indicating spar and microspar. The complex samples show much less orange luminescence than micrite-dominated samples. Rather, complex-matrix samples include areas of luminescence and non-luminescence and a variety of luminescence colors, indicating composition changes of the carbonate minerals. The non-luminescent areas are mottled with the matrix and are also found at the center at some of the cracks.

Samples categorized as “other” have matrices that are not micrite dominated, specifically the drilled samples are either clay-dominated (2225 cm) or microspar-dominated (1650 cm). The clay-dominated sample (2225 cm) included large amounts of organic material, indicated by the dark color of the sample. This sample also hosts some spar-filled voids, likely a later phase of calcite. The microspar sample (1650 cm) shows evidence of recrystallization based on a gradient of crystal coarsening from micrite to microspar. Care was taken to sample the micrite (likely the original carbonate phase) throughout the samples to obtain data consistent with the conditions of deposition. Sample 1650 as it shows the highest carbonate carbon isotope values suggesting this

sample is within the C10 positive isotope excursion. This is consistent with the organic carbon isotope chemostratigraphic record.

Micritic phases, which are seen in all three sample categories, are thought to be a primary phase of calcite that are a result of the pedogenic environments. Spar and microspar are thought to be later phase calcite and occur due to replacement of the original calcite mainly within cracks and voids. These phases are present within all three sample categories. Chalcedony appears to be the youngest mineral phase present within these samples, it is the result of dissolution and replacement of the spar and microspar.

5.1.3 Chemostratigraphy

Segment I encompasses the area that has been interpreted to be the C8 isotope segment, which is a negative trend (Bralower et al., 1999). The C8 isotope segment correlates to other known locations of the C8 isotope segement within the CMF due to the segment showing little variation in value above the base of the section. Segment II and segment III show a sharp increase followed by a sharp decrease of values which can be related to the C9 isotope segment. Segments IV and V show the most enriched values which can be correlated to the C10 positive isotope segment. Segments VI, VII and VIII follow trends, specifically an overall decrease from the sustained positive values, seen in data from Ludvigson et al. (2015) and McColloch (2019) which can be correlated with the C11 isotope segment of the late Aptian. The C10 positive isotope excursion is the easiest section to correlate between data from within the CMF and from other areas as it has the largest positive excursion. (Figure 13). Bralower et al. (1999) discussed the C10 isotope excursion in the Santa Rosa Canyon in Mexico. This section shows marine organic carbon isotope values which correlate to the data from this study (Figure 14). Studies from Ludvigson et al. (2010) and McColloch (2019) discuss the location of the C10 positive

isotope excursion within the Cedar Mountain Formation using both organic carbon and carbonate carbon. The study locations within the CMF, Price River and Ruby Ranch Road, have C10 positive isotope excursion intervals that correlate with data found in this study (Figure 13).

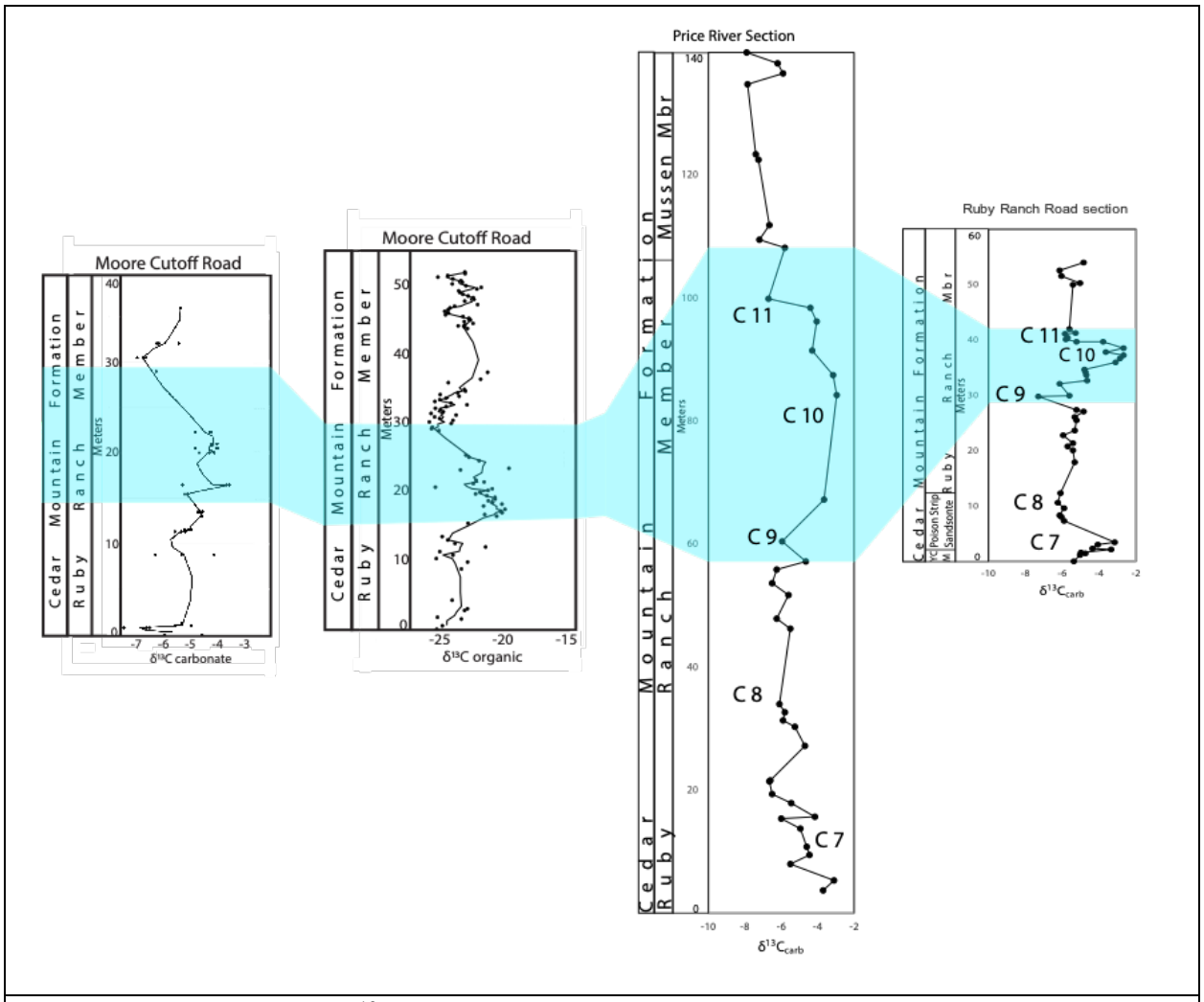

Figure 13: Plots showing $\delta^{13}C$ values at Moore Cutoff Road (Organic (McColloch, 2019) and Carbonate values), Price River (Ludvigson et al., 2015) and Ruby Ranch Road (Ludvigson et al., 2015) correlated across the C10 positive Isotope Excursion

5.2 Discussion

A broad positive isotope excursion (C10) is consistently present in the Ruby Ranch Member of the CMF (Ludvigson et al., 2010; Montgomery 2014; McColloch 2019). Ludvigson et al. (2010) produced chemostratigraphic profiles for multiple locations (Ruby Ranch Road, Price River) within the Ruby Ranch Member and identified the C10 positive isotope excursion (Bralower et al. 1999) within each section using carbonate carbon and organic carbon isotope analysis. A similar positive excursion can be correlated to the positive isotope excursion between 1547 cm and 2000 cm (segments IV and V) found at Moore Cutoff Road. This suggests the C10 positive isotope excursion is a consistent feature across the extent of the Ruby Ranch Member. This positive isotope excursion can also be identified in sections outside of the CMF such as the Santa Rosa Canyon in Mexico and can be correlated to the CMF (Bralower et al., 1999) (Figure 14).

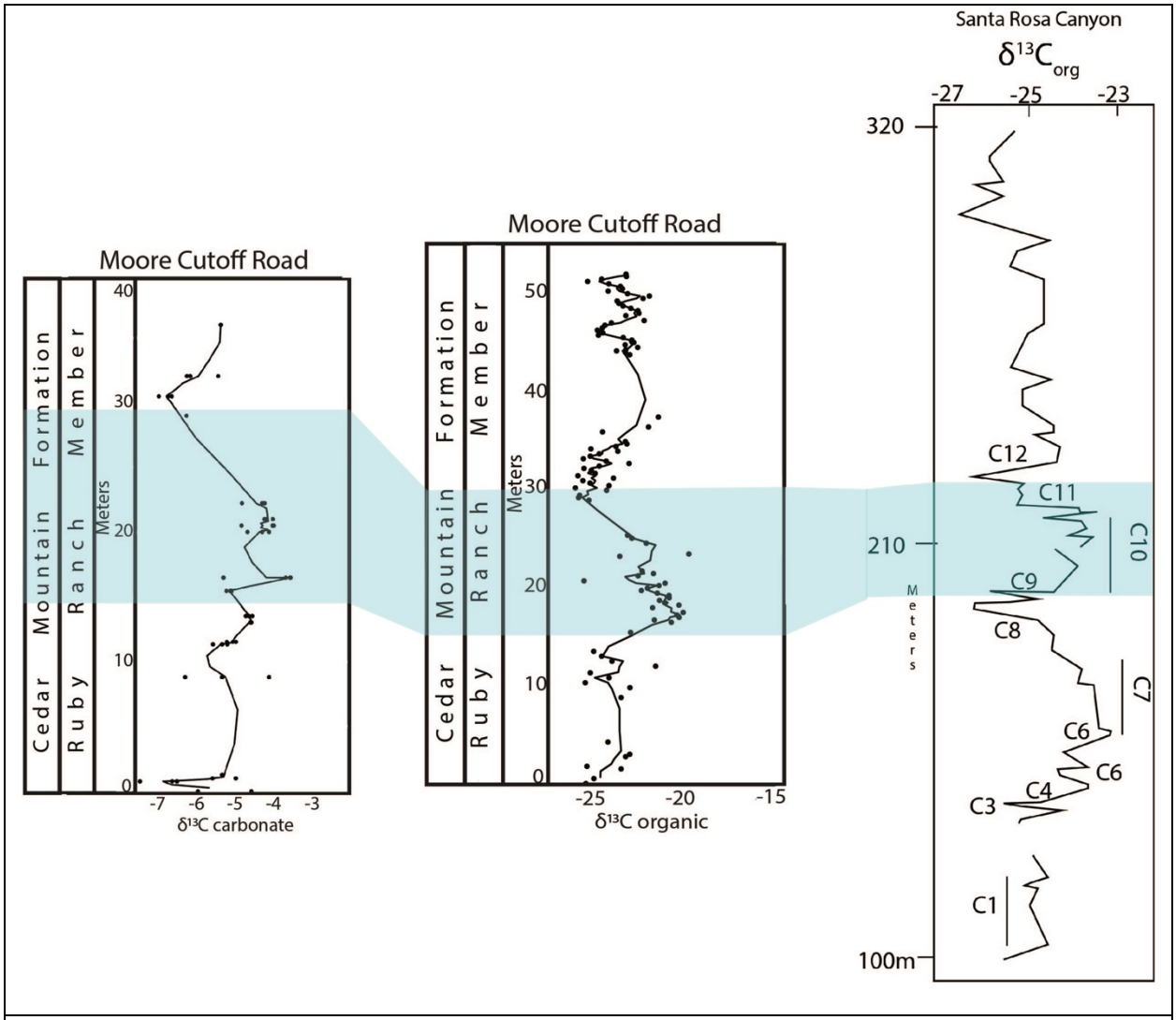

Figure 14: Plots showing Moore Cutoff Road (organic (McColloch, 2019) and carbonate) and Santa Rosa Canyon (Bralower et al. 1999) carbon isotope data correlated across the C10 positive isotope excursion

Temperature data has been collected and analyzed in multiple studies for the Cretaceous time period. McAnena et al. (2013) reported sea surface temperature data using TEX_{86} (marine organic matter) surrounding the C10 positive isotope excursion, pre-event temperature is reported to be approximatey 32º C. During the C10 positive isotope excursion the temperature drops approximately 4º C reporting a value of approximately 28º C. Barron et al. (1995) also

reports these temperature values reporting sea surface temperatures using nannofossils ranging from approximately 28º C to approximately 32º C.

Based on these studies, the C10 positive isotope excursion is thought to be associated with a decrease in temperature (Bottini et al., 2014). Although this is generally thought to be a cooling event there is evidence of hydrothermal warming periods as well, such as the Paquier event which is associated with as much as an 8º C increase in temperature (Jenkyns, 2010). With the Cretaceous being known for high temperatures the C10 decrease contrasts with the majority of the time period and indicates a shift in the environment.

While these earlier cited studies provide sea surface temperatures, terrestrial-based temperature estimates are less common. Suarez et al. (2020) reported temperature data from the Cedar Mountain Formation at the type section for the Ruby Ranch Member (Ruby Ranch Road, East of this study location) using clumped isotope analyses of terrestrial carbonates. This study reports pre-event temperatures of 38.6º C, during the C10 isotope excursion temperatures decrease to 31.9º C and recover post-event to 32.2º C. Unfortunately, the Moore Cutoff Road location carbonates did not produce useable temperature data, so I am unable to evaluate whether a temperature increase or decrease occurs across the C10 isotope segment at this time.

pCO_2 values are widely reported in studies within the Cedar Mountain Formation and other locations during the Cretaceous. Li et al. (2014) report pCO_2 values between 1000 and 2500 ppmV for locations in Southeastern China using values from calcretes in the area. Ekart et al. (1999) report a pCO_2 value of approximately 1500 ppmV using paleosol carbonates much like this study. Wallmann (2001) reports slightly lower values for pCO_2, using a model, ranging from 700 ppmV to 1500 ppmV. Harper et al. (2021) report the lowest pCO_2 value 397 ppmv using pedogenic carbonate stable isotope data. While Suarez et al. (2020) calculate pCO_2 values for the

Ruby Ranch member across the C10 carbon isotope excursion, due to the large $\Delta^{13}C$, these values are likely overestimates. The studies mentioned did not have high enough resolution to identify any trend related to the C10 positive isotope excursion. This study carefully screened samples to only include $\Delta^{13}C$ values between 14 and 17 ‰ as suggested by Cotton and Sheldon (2012). This results in values between 795 ppmV and 2850 ppmV, but this wide range is due to use of multiple values for S(z) and temperature. Calculations for lower temperature yield results ranging from 795 ppmV to 1804 ppmV, which are very similar to ranges presented in previous studies. The data from this study does not have high enough resolution in sampling density to determine if pCO_2 values have any relationship to the C10 positive isotope excursion. The data points that are available show oscillating high and low pCO_2 values (Figure 12).

6. Conclusions

This study aimed to improve upon the existing chemostratigraphy, thoroughly evaluate the carbonate nodules previously collected for the use of clumped isotope paleothermometry and calculate pCO_2 values. Through this study the chemostratigraphic profile has been improved upon at the Moore Cutoff Road location for the Ruby Ranch Member, data was added to McColloch, 2019 with the inclusion of the carbonate carbon isotope work and the completion of the organic carbon isotope work at the top of the section, creating a more complete profile.

Carbonate nodules were used for clumped isotope paleothermometry. While they did not produce interpretable data, they will be re-run with an updated industry standard (Bernasconi et al., 2021) and more sample. Along with the original samples submitted for clumped isotope analysis, additional samples could provide a more complete understanding of temperature throughout the entire section.

The paleoclimate data, including temperature fluctuations and concentration of CO_2, can be related to current conditions and future conditions. The warm climate in the Cretaceous period can be used as an analog for future Earth conditions, which makes it an important time period to study. As the temperature continues to increase at a rapid rate, having knowledge of how the temperature change impacted the environmental conditions during the Cretaceous could be an invaluable tool for determining what needs to be considered for the future.

Appendix A

Table 2: Field Notes and Unit Descriptions (McColloch, 2019)

Unit No.	Description	Sample Name	Unit Thickness (cm)
1	Reddish-gray silty mudstone, not well indurated	MCR-RR-2017-025 MCR-RR-2017-050	34
2	Reddish-gray silty mudstone, peanut to grape sized calcareous nodules	MCR-RR-2017-075 MCR-RR-2017-100 MCR-RR-2017-125 MCR-RR-2017-150	155
3	Poorly lithified mudstone, reddish gray slightly calcareous	(No Sample)	13
4	Sandy, slightly calcareous mudstone, reddish-gray with greenish-gray mottles	MCR-RR-2017-175 MCR-RR-2017-225 MCR-RR-2017-250	92
5	Hardy, sandy limestone, nodular bedded. Pinkish with green mottles. Some chert pebbles present	MCR-RR-2017-275 MCR-RR-2017-300	58
6	Blocky, reddish-gray calcareous, silty sandy mudstone, greenish gray mottles	MCR-RR-2017-325	69
7	Poorly lithified calcareous mudstone, reddish gray with few mottles; . Interbedded with thin nodular calcareous sandstone	MCR-RR-2017-400 MCR-RR-2017-425	49
8	Thin bedded to nodular bedded pink calcareous fine quartz sand stone at base, then less well lithified white-greenish calcareous sandstone capped by hard massive white greenish gray calcareous sandstone	MCR-RR-2017-450 MCR-RR-2017-475 MCR-RR-2017-500 MCR-RR-2017-525	109
9	Unconsolidated muddy sandy, fissile, greenish-gray muddy calcareous	MCR-RR-2017-730 MCR-RR-2017-755 MCR-RR-2017-805	125

	fine sand stone with red-gray mottles		
10	Well-indurated calcareous, light greenish gray fine quartz sandstone grading to purple sandy mudstone with pink and green walnut-sized nodules	MCR-RR-2017-830 MCR-RR-2017-880 MCR-RR-2017-961	176
11	Reddish-gray limestone, also, reddish gray mudstone with carbonate nodules and light greenish gray mottles	MCR-RR-2017-982 MCR-RR-2017-1032 MCR-RR-2017-1082	133
12	Very fine calcareous mudstone, greenish-gray with carbonate nodules grading to nodular limestone	MCR-RR-2017-1132 MCR-RR-2017-1152 MCR-RR-2017-1202 MCR-RR-2017-1252 MCR-RR-2017-1302	187
13	Large softball sized nodules with light reddish gray unconsolidated mudstone grading to coalesced nodular limestone	MCR-RR-2017-1352	50
14	Medium to fine unconsolidated greenish gray sandstone	(No Sample)	195
15	thick, hard, ridge forming nodular limestone, gray, weathered orangish	MCR-RR-2017-1547	33
16	Dark purplish gray calcareous smectitic mudstone with carbonate nodules and faint green mottles, grading to dark gray mudstone with slickensides and red and orange mottles and carbonate nodules.	MCR-RR-2017-1650 MCR-RR-2017-1675 MCR-RR-2017-1700 MCR-RR-2017-1725 MCR-RR-2017-1750 MCR-RR-2017-1775 MCR-RR-2017-1800 MCR-RR-2017-1825 MCR-RR-2017-1850 MCR-RR-2017-1875 MCR-RR-2017-1900 MCR-RR-2017-1925 MCR-RR-2017-1950	312

17	Hard, calcareous, quartz sandstone	MCR-RR-2017-1975	58
18	Calcareous, black sandy carbonate nodule in black sandy mudstone	MCR-RR-2017-2025 MCR-RR-2017-2050 MCR-RR-2017-2075	68
19	Calcareous, black sandy mudstone, with pea sized carbonate nodules	MCR-RR-2017-2100 MCR-RR-2017-2125 MCR-RR-2017-2150 MCR-RR-2017-2175	92
20	Gray-black unconsolidated mudstone with carbonate nodules, red-orange mottles	MCR-RR-2017-2200 MCR-RR-2017-2225	59
21	Sandy, gray, unconsolidated sandy mudstone, with carbonate nodules	MCR-RR-2017-2275	45
22	Poorly lithified, discontinuous limestone, with unconsolidated sand	MCR-RR-2017-2325	60
23	Non resistant conglomerate pinching out with sandstone	MCR-RR-2017-2350	32
24	Poorly lithified conglomerate sandstone	(No Sample)	73
25	Horizontal bedded, calcareous, fine quartz sandstone, thin bedded cross laminated calcareous	MCR-RR-2017-2459 MCR-RR-2017-2509 MCR-RR-2017-2541	123
26	Light tan to nodular limestone to tan, calcareous, mudstone, some orange mottles, slight bedding	MCR-RR-2017-2900 MCR-RR-2017-2925 MCR-RR-2017-2950 MCR-RR-2017-2975 MCR-RR-2017-3000	130
27	Resistant bed, tan, calcareous sand stone with peanut sized carbonate nodules	MCR-RR-2017-3025 MCR-RR-2017-3050 MCR-RR-2017-3075	69
28	Greenish-gray, calcareous, sandy mudstone with peanut sized carbonate nodules	MCR-RR-2017-4000 MCR-RR-2017-4025	29

29	Tan-gray calcareous sandy mudstone, resistant	MCR-RR-2017-4050	46
		MCR-RR-2017-4075	
		MCR-RR-2017-5000	
30	Purple, dark green, mottled calcareous blocky mudstone, pea sized carbonate nodules	MCR-RR-2017-5005	11
		MCR-RR-2017-5025	
		MCR-RR-2017-5050	
		MCR-RR-2017-5075	
31	Tan calcareous muddy sandstone with small limestone bed	MCR-RR-2017-5100	475
		MCR-RR-2017-5125	
		MCR-RR-2017-5150	
		MCR-RR-2017-5175	
		MCR-RR-2017-5200	
		MCR-RR-2017-5225	
		MCR-RR-2017-5275	
		MCR-RR-2017-5300	
		MCR-RR-2017-5350	
		MCR-RR-2017-5400	
		MCR-RR-2017-5450	
		MCR-RR-2017-5500	
		MCR-RR-2017-5550	
		MCR-RR-2017-6000	250
		MCR-RR-2017-6150	
		MCR-RR-2017-6200	
		MCR-RR-2017-6250	

Table 3: Field Notes and Unit Description, 2020

Unit No.	Description	Sample Name(s)	Unit Thickness (cm)
1	Grey silty mudstone with pea sized carbonate nodules, some orange mottles	MCR-RR-2020-0 MCR-RR-2020-25 MCR-RR-2020-40 MCR-RR-2020-50 MCR-RR-2020-75 MCR-RR-2020-100 MCR-RR-2020-125 MCR-RR-2020-150 MCR-RR-2020-175 MCR-RR-2020-200 MCR-RR-2020-225 MCR-RR-2020-250 MCR-RR-2020-275 MCR-RR-2020-300	735

		MCR-RR-2020-325 MCR-RR-2020-350 MCR-RR-2020-375 MCR-RR-2020-400 MCR-RR-2020-425 MCR-RR-2020-450 MCR-RR-2020-475 MCR-RR-2020-500 MCR-RR-2020-525 MCR-RR-2020-550 MCR-RR-2020-575 MCR-RR-2020-600 MCR-RR-2020-625 MCR-RR-2020-650 MCR-RR-2020-675 MCR-RR-2020-700 MCR-RR-2020-725	
2	Orange grey siltstone, heavily mottled, mudcracks present	MCR-RR-2020-750	17
3	Grey silty mudstone, orange mottles, some iron oxide staining	MCR-RR-2020-775 MCR-RR-2020-800 MCR-RR-2020-825	73

Appendix B

Table 4: Unit Thickness 2017 vs. 2020

Sample Name	2017 Thickness from base of RRM (cm)	2020 Thickness from base of RRM (cm)
MCR-RR-2017-25	25	25
MCR-RR-2017-50	50	50
MCR-RR-2017-75	75	75
MCR-RR-2017-100	100	100
MCR-RR-2017-125	125	125
MCR-RR-2017-150	150	150
MCR-RR-2017-175	175	175
MCR-RR-2017-225	225	225
MCR-RR-2017-250	250	250
MCR-RR-2017-275	275	275
MCR-RR-2017-300	300	300
MCR-RR-2017-325	325	325
MCR-RR-2017-400	400	400
MCR-RR-2017-425	425	425
MCR-RR-2017-450	450	450

MCR-RR-2017-475	475	475
MCR-RR-2017-500	500	500
MCR-RR-2017-525	525	525
MCR-RR-2017-730	730	730
MCR-RR-2017-755	755	755
MCR-RR-2017-805	805	805
MCR-RR-2017-830	830	830
MCR-RR-2017-880	880	880
MCR-RR-2017-961	961	961
MCR-RR-2017-982	982	982
MCR-RR-2017-1032	1032	1032
MCR-RR-2017-1082	1082	1082
MCR-RR-2017-1132	1132	1132
MCR-RR-2017-1152	1152	1152
MCR-RR-2017-1202	1202	1202
MCR-RR-2017-1252	1252	1252
MCR-RR-2017-1302	1302	1302
MCR-RR-2017-1352	1352	1352
MCR-RR-2017-1547	1547	1547
MCR-RR-2017-1650	1650	1650
MCR-RR-2017-1675	1675	1675
MCR-RR-2017-1700	1700	1700
MCR-RR-2017-1725	1725	1725
MCR-RR-2017-1750	1750	1750
MCR-RR-2017-1800	1800	1800
MCR-RR-2017-1825	1825	1825
MCR-RR-2017-1850	1850	1850
MCR-RR-2017-1875	1875	1875
MCR-RR-2017-1900	1900	1900
MCR-RR-2017-1925	1925	1925
MCR-RR-2017-1950	1950	1950
MCR-RR-2017-1975	1975	1975
MCR-RR-2017-2000	2000	2000
MCR-RR-2017-2025	2025	2025
MCR-RR-2017-2050	2050	2050
MCR-RR-2017-2075	2075	2075
MCR-RR-2017-2100	2100	2100
MCR-RR-2017-2125	2125	2125
MCR-RR-2017-2150	2150	2150
MCR-RR-2017-2175	2175	2175
MCR-RR-2017-2200	2200	2200
MCR-RR-2017-2225	2225	2225
MCR-RR-2017-2275	2275	2275
MCR-RR-2017-2325	2325	2325
MCR-RR-2017-2350	2350	2350

MCR-RR-2017-2459	2459	2459
MCR-RR-2017-2509	2509	2509
MCR-RR-2017-2900	2900	2900
MCR-RR-2017-2925	2925	2925
MCR-RR-2017-2950	2950	2950
MCR-RR-2017-2975	2975	2975
MCR-RR-2017-3000	3000	3000
MCR-RR-2017-3025	3025	3025
MCR-RR-2017-3050	3050	3050
MCR-RR-2017-3075	3075	3075
MCR-RR-2017-4000	4000	3100 ***adjusted measurements***
MCR-RR-2017-4025	4025	3125
MCR-RR-2017-4050	4050	3150
MCR-RR-2017-4075	4075	3175
MCR-RR-2017-5000	5000	3200
MCR-RR-2017-5005	5005	3205
MCR-RR-2017-5025	5025	3225
MCR-RR-2017-5050	5050	3250
MCR-RR-2017-5075	5075	3275
MCR-RR-2017-5100	5100	3300
MCR-RR-2017-5125	5125	3325
MCR-RR-2017-5150	5150	3350
MCR-RR-2017-5175	5175	3375
MCR-RR-2017-5200	5200	3400
MCR-RR-2017-5225	5225	3425
MCR-RR-2017-5250	5250	3450
MCR-RR-2017-5275	5275	3475
MCR-RR-2017-5300	5300	3500
MCR-RR-2017-5400	5400	3600
MCR-RR-2017-5450	5450	3650
MCR-RR-2017-5550	5550	3750

Table 5: Facies Descriptions

Facies	Description	Samples
1	Reddish-grey sandy calcareous mudstone w/ carbonate nodules and green mottles	MCR-RR-2017-0 MCR-RR-2017-75 MCR-RR-2017-100 MCR-RR-2017-125 MCR-RR-2017-150 MCR-RR-2017-175 MCR-RR-2017-225 MCR-RR-2017-250 MCR-RR-2017-275 MCR-RR-2017-300

		MCR-RR-2017-325 MCR-RR-2017-400 MCR-RR-2017-425 MCR-RR-2017-1032 MCR-RR-2017-1082
2	Grey sandy calcareous shale w/ carbonate nodules	MCR-RR-2017-450 MCR-RR-2017-475 MCR-RR-2017-500 MCR-RR-2017-525
3	Greenish fine sandstone	MCR-RR-2017-730 MCR-RR-2017-755 MCR-RR-2017-805 MCR-RR-2017-830
4	Grey to black calcareous mudstone w/ carbonate nodules	MCR-RR-2017-1132 MCR-RR-2017-1152 MCR-RR-2017-1202 MCR-RR-2017-1252 MCR-RR-2017-1302 MCR-RR-2017-1650 MCR-RR-2017-1675 MCR-RR-2017-1700 MCR-RR-2017-1725 MCR-RR-2017-1750 MCR-RR-2017-1775 MCR-RR-2017-1800 MCR-RR-2017-1825 MCR-RR-2017-1850 MCR-RR-2017-1875 MCR-RR-2017-1900 MCR-RR-2017-1925 MCR-RR-2017-1950 MCR-RR-2017-2025 MCR-RR-2017-2050 MCR-RR-2017-2075 MCR-RR-2017-2100 MCR-RR-2017-2125 MCR-RR-2017-2150 MCR-RR-2017-2175 MCR-RR-2017-2200 MCR-RR-2017-2225 MCR-RR-2017-2275 MCR-RR-2017-2325 MCR-RR-2017-2350 MCR-RR-2017-2459 MCR-RR-2017-2509 MCR-RR-2017-2541

5	Green-grey sandstone	MCR-RR-2017-1352 MCR-RR-2017-1547
6	Coalesced carbonate nodules	No Sample
7	Tan resistant calcareous sandstone	MCR-RR-2017-1975
8	Tan-yellow sandy mudstone w/ orange mottles and carbonate nodules	MCR-RR-2017-2900 MCR-RR-2017-2925 MCR-RR-2017-2950 MCR-RR-2017-2975 MCR-RR-2017-3000 MCR-RR-2017-3025 MCR-RR-2017-3050 MCR-RR-2017-3075
9	Grey sandy calcareous mudstone w/ carbonate nodules	MCR-RR-2017-4000 MCR-RR-2017-4025 MCR-RR-2017-4050 MCR-RR-2017-4075 MCR-RR-2017-5000
10	Purple-green mottled calcareous mudstone w/ carbonate nodules	MCR-RR-2017-880 MCR-RR-2017-961 MCR-RR-2017-982 MCR-RR-2017-5005 MCR-RR-2017-5025
11	Green-grey sandy mudstone w/ carbonate nodules, orange resistant nodules and orange & green mottles	MCR-RR-2020-0 MCR-RR-2020-25 MCR-RR-2020-40 MCR-RR-2020-50 MCR-RR-2020-75 MCR-RR-2020-100 MCR-RR-2020-125 MCR-RR-2020-150 MCR-RR-2020-175 MCR-RR-2020-200 MCR-RR-2020-250 MCR-RR-2020-275 MCR-RR-2020-300 MCR-RR-2020-325 MCR-RR-2020-350 MCR-RR-2020-375 MCR-RR-2020-400 MCR-RR-2020-425 MCR-RR-2020-450 MCR-RR-2020-475 MCR-RR-2020-500 MCR-RR-2020-525 MCR-RR-2020-550 MCR-RR-2020-575

		MCR-RR-2020-600 MCR-RR-2020-625 MCR-RR-2020-650 MCR-RR-2020-700 MCR-RR-2020-800 MCR-RR-2020-825
12	Tan sandy mudstone	MCR-RR-2017-5075 MCR-RR-2017-5100 MCR-RR-2017-5125 MCR-RR-2017-5150 MCR-RR-2017-5175 MCR-RR-2017-5200 MCR-RR-2017-5225 MCR-RR-2017-5275 MCR-RR-2017-5300 MCR-RR-2017-5350 MCR-RR-2017-5400 MCR-RR-2017-5450 MCR-RR-2017-5500 MCR-RR-2017-5550 MCR-RR-2017-6000 MCR-RR-2017-6150 MCR-RR-2017-6200 MCR-RR-2017-6250 MCR-RR-2020-725 MCR-RR-2020-750 MCR-RR-2020-775

Appendix C

Table 6: Stable Isotope Data

Sample Name	Petrography	CL Imaging	$\delta^{13}C$ Value (‰)	$\delta^{18}O$ Value (‰)
MCR-RR-2017-75	Micrite and microspar	*N/A*	Avg: -6.85	Avg: -7.88
MCR-RR-2017-75			-6.49	-8.49
MCR-RR-2017-75			-7.45	-7.59
MCR-RR-2017-75			-6.61	-7.57
MCR-RR-2017-100	Micrite		Avg: -5.25	Avg: -7.61
MCR-RR-2017-100			-4.95	-7.50
MCR-RR-2017-100			-5.56	-7.72
MCR-RR-2017-125		*N/A*	Avg: -5.31	Avg: -8.85
MCR-RR-2017-880	Micrite, spar and microspar		Avg: -5.22	Avg: -8.44
MCR-RR-2017-880			-4.09	-8.17

MCR-RR-2017-880			-5.31	-8.25
MCR-RR-2017-880			-6.27	-8.89
MCR-RR-2017-1132	Fiberous chert, micrite	*N/A*	Avg: -5.34	Avg: -8.84
MCR-RR-2017-1132			-5.31	-8.86
MCR-RR-2017-1132			-5.54	-9.02
MCR-RR-2017-1132			-5.17	-8.65
MCR-RR-2017-1152	Homogenous micrite		Avg: -5.05	Avg: -8.82
MCR-RR-2017-1152			-4.95	-8.92
MCR-RR-2017-1152			-5.03	-8.78
MCR-RR-2017-1152			-5.18	-8.76
MCR-RR-2017-1302	Micrite dominated	*N/A*	Avg: -4.55	Avg: -7.85
MCR-RR-2017-1302			-4.57	-7.82
MCR-RR-2017-1302			-4.54	-7.87
MCR-RR-2017-1352	Complex, micrite, spar		Avg: -4.61	Avg: -8.29
MCR-RR-2017-1352			-9.50	-9.03
MCR-RR-2017-1352			-4.61	-8.20
MCR-RR-2017-1352			-4.69	-8.00
MCR-RR-2017-1352			-4.52	-7.94
MCR-RR-2017-1547	Micrite dominated		Avg: -5.12	Avg: -8.11
MCR-RR-2017-1547			-5.10	-8.07
MCR-RR-2017-1547			-5.20	-8.04
MCR-RR-2017-1547			-5.06	-8.23
MCR-RR-2017-1650	Microspar	*N/A*	Avg: -3.99	Avg: -8.58
MCR-RR-2017-1650			-3.53	-8.58
MCR-RR-2017-1650			-3.52	-8.60
MCR-RR-2017-1650			-3.65	-8.60
MCR-RR-2017-1650			-5.27	-8.54
MCR-RR-2017-2000	Homogenous micrite w evidence of fossils	*N/A*	Avg: -4.33	Avg: -8.40
MCR-RR-2017-2000			-4.65	-8.63
MCR-RR-2017-2000			-4.27	-8.29
MCR-RR-2017-2000			-4.08	-8.29
MCR-RR-2017-2050	Micrite, spar	*N/A*	-4.25	-8.97
MCR-RR-2017-2050			-4.00	-8.89
MCR-RR-2017-2050			-4.80	-9.37
MCR-RR-2017-2050			-3.96	-8.64
MCR-RR-2017-2100	Micrite dominated with spar	*N/A*	-4.11	-8.23
MCR-RR-2017-2100			-4.15	-8.35
MCR-RR-2017-2100			-4.21	-8.31
MCR-RR-2017-2100			-3.98	-8.02
MCR-RR-2017-2225	Siliciclastic dominated	*N/A*	-4.42	-8.69
MCR-RR-2017-2225			-4.20	-8.43
MCR-RR-2017-2225			-4.26	-8.49
MCR-RR-2017-2225			-4.79	-9.14

MCR-RR-2017-3050	Micrite dominated	*N/A*	-6.76	-8.56
MCR-RR-2017-3050			-6.96	-8.81
MCR-RR-2017-3050			-6.71	-8.48
MCR-RR-2017-3050			-6.62	-8.40
MCR-RR-2017-3205	Micrite dominated	*N/A*	-5.93	-8.48
MCR-RR-2017-3205			-6.23	-8.59
MCR-RR-2017-3205			-6.14	-8.42
MCR-RR-2017-3205			-5.41	-8.42
MCR-RR-2017-3600	Micrite dominated	*N/A*	-5.34	-8.58
MCR-RR-2017-3600			-5.34	-8.87
MCR-RR-2017-3600			-5.34	-8.29

Table 7: pCO_2 Data

Sample	Temperature	S(z) Value	pCO_2 (ppm)
1547	25	4000	1007.56
1650	25	4000	857.21
2000	25	4000	1030.98
2050	25	4000	795.79
3050	25	4000	858.72
1547	25	7000	1763.23
1650	25	7000	1500.11
2000	25	7000	1804.22
2050	25	7000	1392.63
3050	25	7000	1502.77
1547	39	4000	1555.71
1650	39	4000	1399.47
2000	39	4000	1631.13
2050	39	4000	1340.16

3050	39	4000	1343.92
1547	39	7000	2718.40
1650	39	7000	2445.19
2000	39	7000	2850.23
2050	39	7000	2341.24
3050	39	7000	2347.87

Table 8: Clumped Isotope Data

Sample	Yield	$\delta^{18}O$	$\delta^{13}C$	D47	Temperature (ºC)
100	13.3	-9.53519	-6.60310	-0.28227	34.6
1152	32.4	-8.67496	-4.34177	-0.3063	56.5
1152	24.9	-8.63421	-4.43791	-0.28959	47.8
1547	36.3	-8.73902	-4.28739	-0.32037	64.2

Appendix D

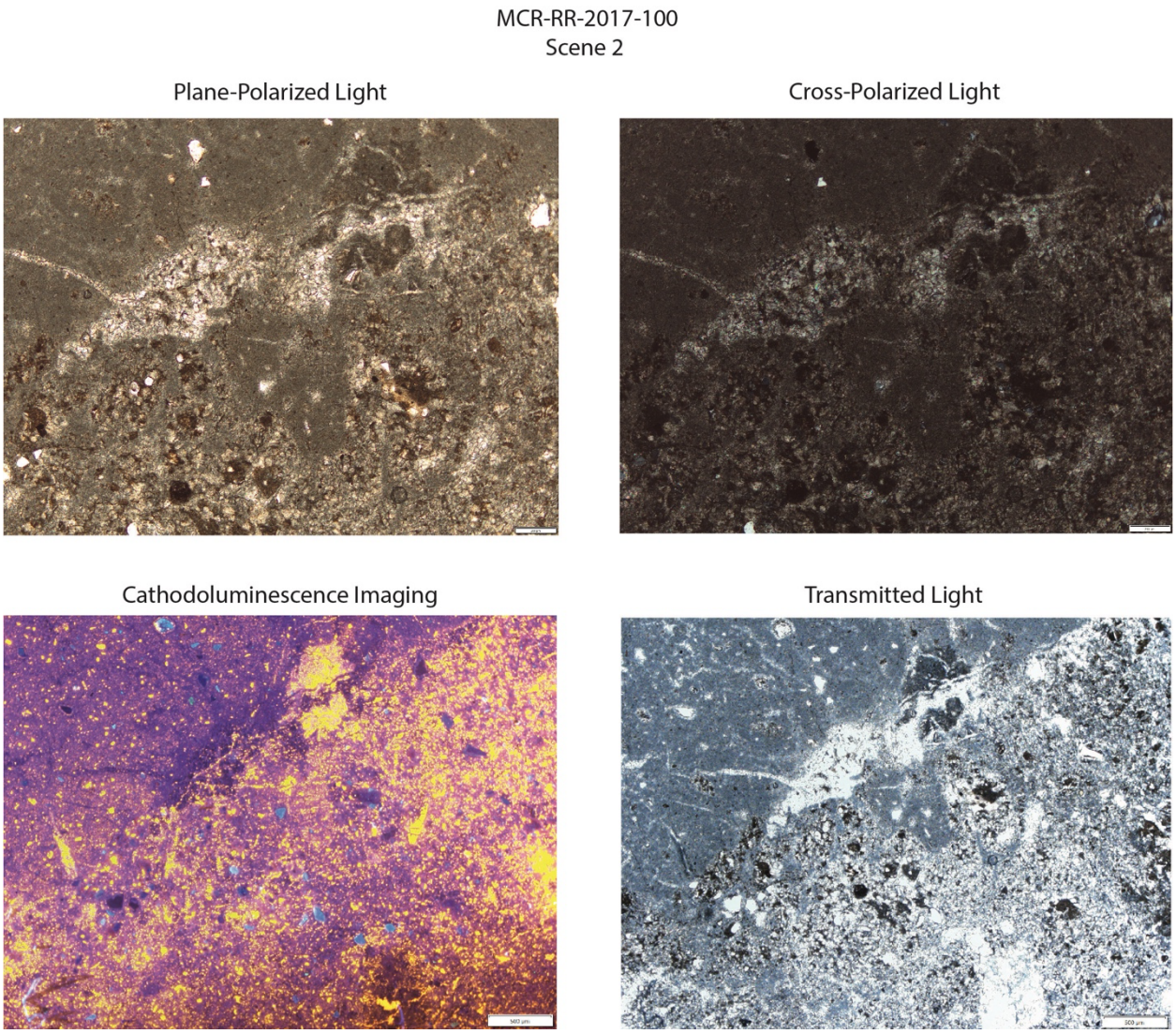

Figure 15: Sample 100 (scene 2 of 2)), which is categorized as micrite-dominated, shown in Cross-Polarized light, Plane-Polarized light, Cathodoluminescence Imaging and Transmitted light. Cathodoluminescence Imaging and Transmitted light photos are taken with a 500 µm scale while the Plane-Polarized and Cross-Polarized photos are taken with a 200 µm scale.

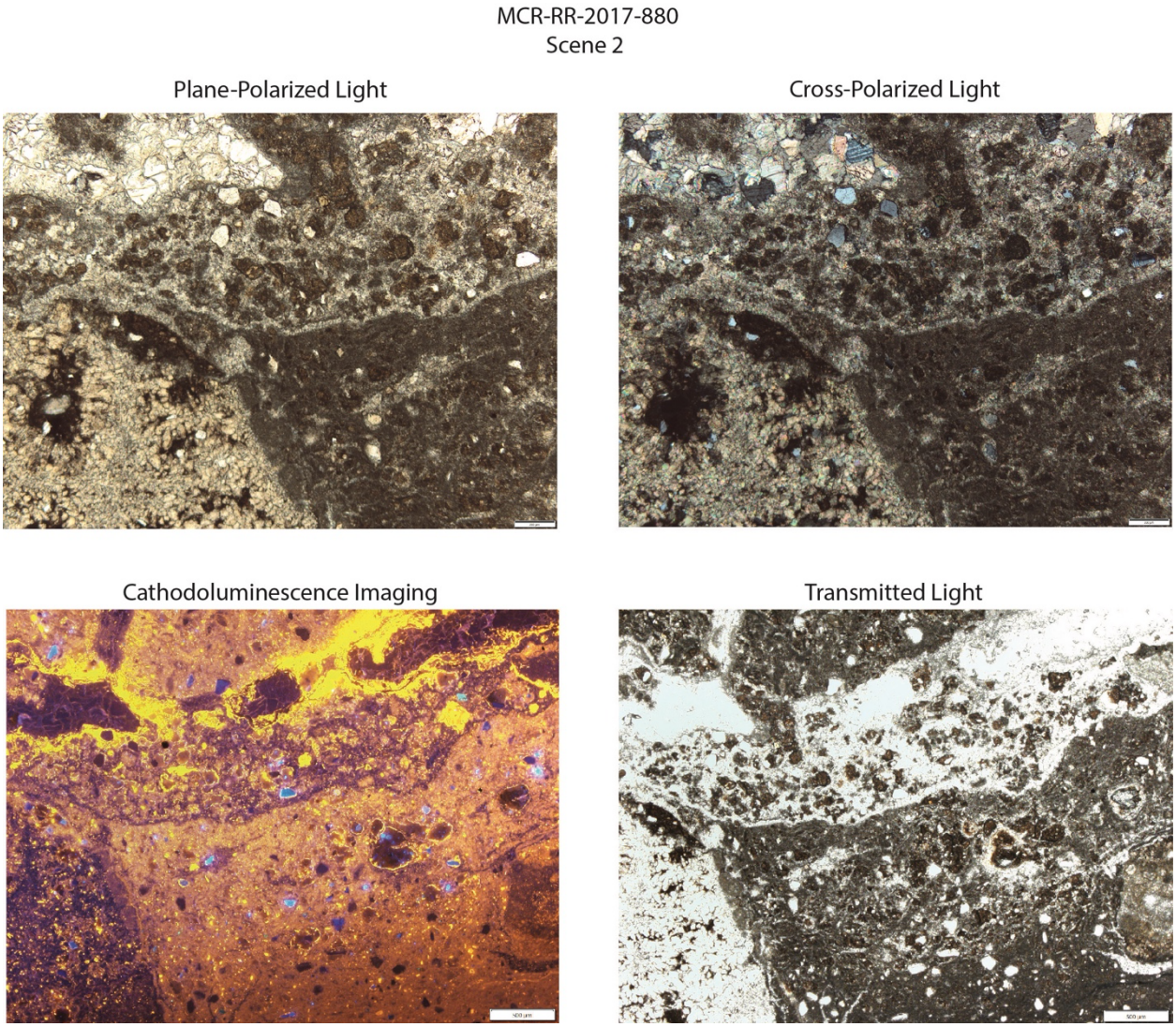

Figure 16: Sample 880 (scene 2 of 2)), which is categorized as a complex matrix, shown in Cross-Polarized light, Plane-Polarized light, Cathodoluminescence Imaging and Transmitted light. Cathodoluminescence Imaging and Transmitted light photos are taken with a 500 µm scale while the Plane-Polarized and Cross-Polarized photos are taken with a 200 µm scale.

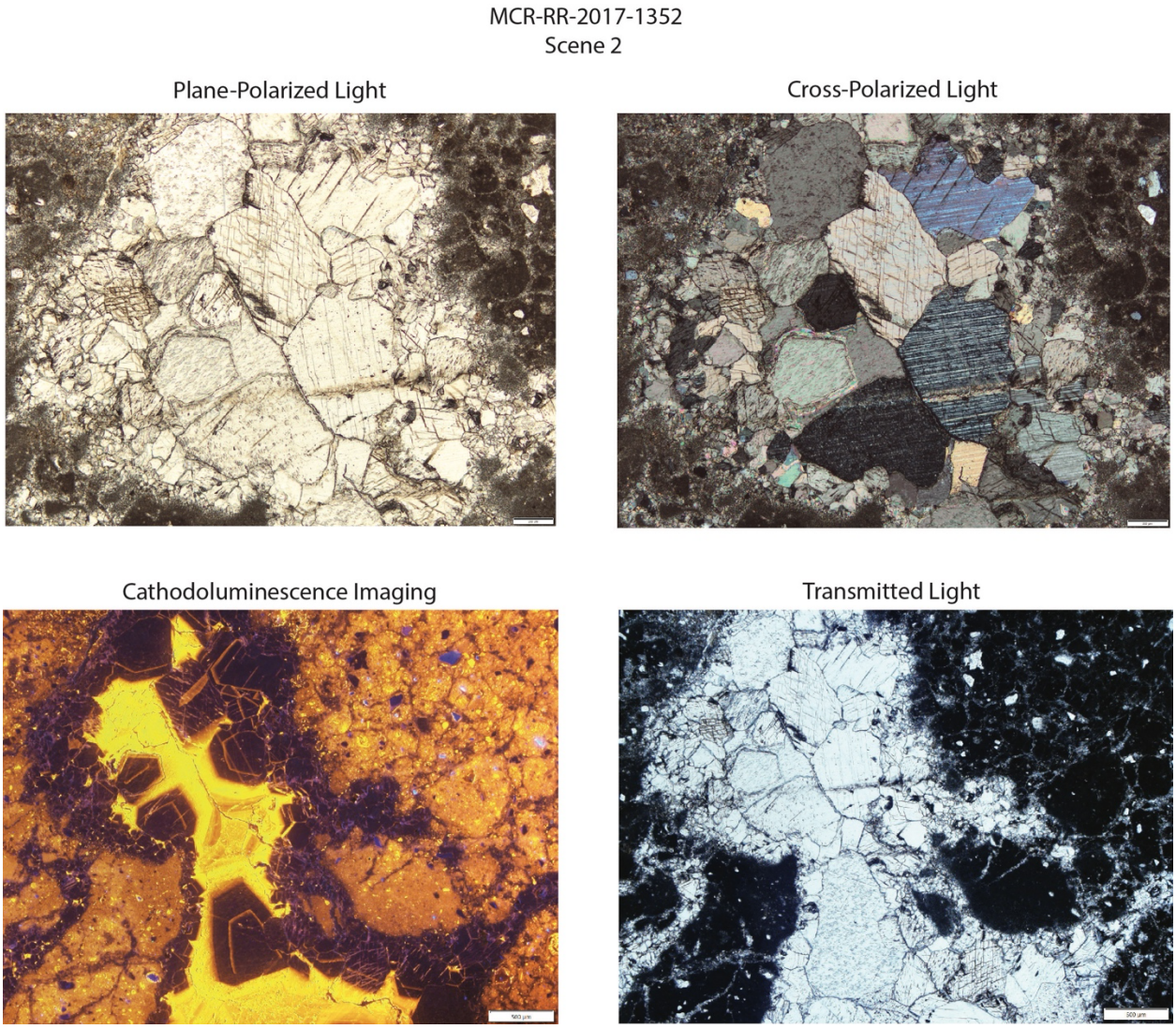

Figure 17: Sample 1352 (scene 2 of 2)), which is categorized as a complex matrix, shown in Cross-Polarized light, Plane-Polarized light, Cathodoluminescence Imaging and Transmitted light. Cathodoluminescence Imaging and Transmitted light photos are taken with a 500 µm scale while the Plane-Polarized and Cross-Polarized photos are taken with a 200 µm scale.

References

Affek, H.P., 2012, Clumped isotope paleothermometry: principles, applications and challenges: Paleontological Society, v. 18, p. 101-114.

Barron, E.J., Fawcett, P.J., Peterson, W.H., 1995, A "simulation" of mid-Cretaceous climate: Paleoceanography, v. 10, no. 5, p. 953-962.

Bernasconi, S., Daëron, M., Bergmann, K., Bonifacie, M., Meckler, A.N. et al., 2021, InterCarb: A community effort to improve inter-laboratory standardization of the carbonate clumped isotope thermometer using carbonate standards: hal-03094122.

Bodin, S., Meissner, P., Janssen, N.M.M., Steuber, T., Mutterlose, J., 2015, Large igneous provinces and organic carbon burial: Controls on global temperature and continental weathering during the early Cretaceous Global and Planetary Change, v. 133, p. 238 - 253.

Bralower, T.J., CoBabe, E., Clement, B., Sliter, W.V., Osburn, C.L., Longoria, J., 1999, The record of global change in Mid-Cretaceous (Barremian - Albian) sections from the Sierra Madre, Northeastern Mexico Journal of Formainiferal Research v. 29, p. 418-437.

Bottini, C., Erba, E., Tiraboschi, D., Jenkyns, H.C., Schouten, S., Sinninghe Damsté, J.S., 2014, Climate variability and relationship with ocean fertility during the Aptian Stage: Climate of the Past, v. 10, p. 689-738.

Bottini, C., Erba, E., 2018, Mid-Cretaceous Paleoenvironmental Changes in the Western Tethys: Climate of the Past, v. 14, p. 1147 - 1163.

Cotton, J.M., Sheldon N.D., 2012, New constraints on using paleosols to reconstruct atmospheric pCO_2 : Geological Society of America, v. 124, no. 9/10, p. 1411–1423.

Dennis, K.J., Affek, H.P., Passey, B.H., Schrag, D.P., Eiler, J.M. , 2011, Defining an absolute reference frame for 'clumped' isotope studies of CO2: Geochimica et Cosmochimica Acta v. 75, no. 22, p. 7117-7131.

Eiler, J.M., 2011, Paleoclimate reconstruction using carbonate clumped isotope themometry: Quaternary Science Reviews, v. 30, p. 3575-3588.

Ekart D.D., Cerling T.E., Montañez I.P., Tabor N.J., 1999, A 400 million year carbon isotope record of pedogenic carbonate: Implications for paleoatmospheric carbon dioxide: American Journal of Science, v. 299, p. 805-827.

Harper D.T., Suarez, M.B., Uglesuch, J., You, H., Li, D., Dodson, P., 2021, Aptian-Albian clumped isotopes from northwest China: cool temperatures, variable atmospheric pCO_2 and regional shifts in the hydrologic cycle: Climate of the past, v. 17, p. 1607-1625.

Hay, W.W., 2011, Can humans force a return to a 'Cretaceous' climate?: Sedimentary Geology, v. 235, p. 5-26.

Hemming, N.G., Meyers, W.J., Grams, J.C., 1989, Cathodoluminescence in diagenetic calcites: the roles of Fe and Mn as deduced from electron probe and spectrophotometric measurements: Journal of Sedimentary Petrology, v. 59, no. 3, p. 404-411.

Jenkyns, H.C., 2010, Geochemistry of ocean anoxic events: Geochemistry, Geophysics, Geosystems v. 11.

Joeckel, R.M., Ludvigson, G.A, Möller, A., Hotton, C.L., Suarez, M.B., Suarez, C.A., Sames, B., Kirkland, J.I., Hendrix, B., 2019, Chronostratigraphy and terrestrial palaeoclimatology of Berriasian-Hauterivian strata of the Cedar Mountain Formation, Utah, USA. The Geological Society of London, v. 498.

Kirkland, J.I., Britt, B., Burge, D.L., Carpenter, K., Cifelli, R., Decourten, F., Eaton, J., Hasiotis, S., Lawton, T., 1997, Lower to middle Cretaceous dinosaur faunas of the central Colorado plateau: A key to understanding 35 million years of tectonics, sedimentology, evolution and biogeography: BYU Geological Studies v. 42, p. 70-103.

Kirkland, J.I., Suarez, M., Suarez, C., Hunt-Foster, R., 2016, The Medial Cretaceous in East-Central Utah - The Cedar Mountain Formation and its bounding strata: Society of Vertebrate Paleontology. Field Trip Guide.

Knight, J.A.,2018, Quantifying climate change over the early Cretaceous Ruby Ranch Member of the Cedar Mountain Formation, East-Central Utah [Masters of Science] University of Texas, San Antonio

Kraus M.J., 1999, Paleosols in clastic sedimentary rocks: their geologic applications: Earth-Science Reviews, v. 47, p. 41-70.

Lee, J., 2020, A novel approach to date continental sediment deposition and paleoclimate events using volcanogenic zircon in paleosols [Masters of Science] Lawrence, University of Kansas.

Li, X., Jenkyns, H.C., Zhang, C., Wang, Y., Liu, L., Cao, K., 2014, Carbon isotope signatures of pedogenic carbonates from SE China: rapid atmospheric pCO_2 changes during middle-late Early Cretaceous time: Geology Magazine, v. 151, p. 830-849.

Li, J., Wen, X.Y., Huang, C.M., 2016, Lower Cretaceous paleosols and paleoclimate in Sichuan Basin, China: Cretaceous Research, v. 62, p. 154-171.

Ludvigson, G.A., Joeckel, R.M., Gonzalez, L.A., Gulbranson, E.L., Rasbury, E.T., Hunt, G.J., Kirkland, J.I., Madsen, S., 2010, Correlation of Aptian-Albian Carbon Isotope Excurisios in Continental Strata of the Cretaceous Foreland Basin, Eastern Utah, U.S.A.: Journal of Sedimentary Reseach, v. 80, p. 955-974.

Ludvigson, G.A., 2015, The emerging terrestrial record of Aptian-Albian global change: Cretaceous Research v. 56, p. 1-24.

Mack, G.H., James, W.C., Monger, H.C., 1993, Classification of paleosols: Geological Society of America, v. 105, p. 129-136.

McAnena, A., Flogel, S., Herrle, J.O., Griesnd, A., Pross, J., Talbot, H.M., Rethemeyer, J.,Wallmann, K., Wagner, T., 2013, Atlantic cooling associated with a marine biotic crisis during the Mid-Cretaceous period: Nature, v. 6.

McColloch, C., 2019, Carbon isotope chemostratigraphy of the Ruby Ranch member of the Cedar Mountain Formation near Moore cut-off road, West Central Utah [Masters of Science] University of Texas, San Antonio.

Montañez, I.P., 2012, Modern soil system constraints on reconstructing deep-time atmosphere CO_2: Geocheimica et Cosmochimica Acta, v. 101, p. 57 – 75.

Montgomery, E.H., 2014, Limnogeology and chemostratigraphy of carbonates and organic carbon from the Cedar Mountain Formation, Eastern Utah [Masters of Science, University of Texas at San Antonio]

Petersen, S.V., Defliese, W.F., Saenger, C. et al., Effects of Improved ^{17}O Correction on Interlaboratory Agreement in Clumped Isotope Calibrations, Estimates of Mineral-Specific Offsets, and Temperature Dependence of Acid Digestion Fractionation: Geochemistry, Geophysics, Geosystems, v. 20, i. 7, p. 3495-3519.

Retallack, G.J., 1999, Postapocalyptic greenhouse paleoclimate revealed by earliest Triassic paleosols in the Sydney Basin, Australia: Geological Society of America Bulletin, v. 111, no. 1, p. 52-70.

Scholle, P.A., Arthur, M.A., 1980, Carbon isotope fluctuations in Cretaceous pelgic limestones: Potential stratigraphic and petroleum exploration: AAPG Bulletin v. 64, p. 67 - 87.

Suarez, M.B., Gonzalez, L.A., Ludvigson, G.A. , 2011, Quantification of a greenhouse hydrologic cycle from equatorial to polar latitudes: The mid - Cretaceous water bearer revisited: Paleogeography, Paleoclimate, Paleoecology, v. 307, p. 301-312.

Suarez, M.B., Knight, J.A., Godet, A., Ludvigson, G.A., Snell, K.E., Murphy, L., Kirkland, J.I., 2020, Multiproxy strategy for determining paleoclimate parameters in the Ruby Ranch Member of the Cedar Mountain Formation, Geological Society, London, Special Publications, v. 507, p. 313-334.

Ufner, D. F., Gonzales, L.A.,Ludvigson, G.A., Brenner, R.L., Witzke, B.J., 2004, Evidence for increased latent heat transport during the Cretaceous (Albian) greenhouse warming Geology, v. 32, p. 1049 - 1052.

Wallmann, K., 2001, Controls on the Cretaceous and Cenozoic evolution of seawater composition, atmospheric CO_2 and climate: Geochimica et Cosmochimica Acta, v. 65, no. 18, p. 3005-3025.